A&A, 715, A39 (2026)
https://doi.org/10.1051/0004-6361/202660937
© The Authors 2026

Astronomy & Astrophysics

Wild behaviour near the finish line: The Type Ibn SN 2020able and its stratified environment

L. Tartaglia[1,⋆], E. Cappellaro[2], G. Valerin[2], A. Pastorello[2], S. Benetti[2], A. Reguitti[2,3], L. Tomasella[2], P. Lundqvist[4], K. Misra[5], A. Gangopadhyay[4], R. Dastidar[3], B. Ailawadhi[6], Dimple[7,8], B. Kumar[9,10], V. K. Jha[11], M. Singh[12], N. Elias-Rosa[2,13], C. P. Gutiérrez[13], D. A. Howell[14,15], D. Hiramatsu[16], C. Pellegrino[17], J. Andrews[19], D. J. Sand[20], N. Smith[20], J. Pearson[20], S. Wyatt[17], P. Ochner[18,2], Y.-Z. Cai (蔡永志)[2,21,22], J. Burke[25], C. McCully[14], M. Newsome[23], and E. Padilla Gonzalez[24]

(Affiliations can be found after the references)

Received 14 May 2026 / Accepted 7 August 2026

ABSTRACT

We present spectrophotometric observations of the Type Ibn supernova SN 2020able, along with a comprehensive analysis and modelling of its evolution. The transient occurred in SDSS J092602.93+243115.1, a faint host galaxy characterised by significantly subsolar metallicity ($12 + \log(\mathrm{O/H}) \simeq 8.28$ dex). The early photometric evolution and high peak luminosity ($L_{peak} \simeq 4.4 \times 10^{43}$ erg s^{-1}) indicate an efficient conversion of ejecta kinetic energy into radiation via interaction with the circumstellar medium. Light-curve modelling suggests that this interaction involves ejecta with a mass of $M_{\rm ej} \simeq 1.3\,M_{\odot}$ impacting a shell of $M_{\rm CSM} \simeq 0.6\,M_{\odot}$. However, interaction is found to be geometrically and temporally confined within a few days after explosion, with the later evolution of the transient being dominated by the free expansion of the ejecta. Spectroscopic analysis reveals a complex, stratified, circumstellar environment. In addition to the innermost shocked region, we identify two additional He-rich shells: a dense inner one ($n_{\rm e} \simeq 1.4 \times 10^{9}$ cm^{-3}) located at $R \gtrsim 9.3 \times 10^{14}$ cm, and a more extended outer component reaching $R_{out} \simeq 3.3 \times 10^{15}$ cm and expanding at approximately 1.2×10^{3} km s^{-1}. The physical parameters of the former suggest it was produced by a discrete, pre-supernova eruptive event similar to that of SN 2006jc, which expelled approximately $1.8 \times 10^{-2}\,M_{\odot}$ of material. Conversely, the expansion velocity of the outermost shell is consistent with the escape velocity of Wolf–Rayet stars, pointing towards a late WN- to WC-type progenitor as the most viable candidate for SN 2020able.

Key words. supernovae: general – supernovae: individual: SN 2020able – supernovae: individual: SN 2010al

1. Introduction

Massive stars are expected to end their lives with spectacular explosions, giving rise to core-collapse supernovae (CC SNe) following the collapse of their iron cores. The observational variety of CC SNe is determined by the composition of the residual envelope at the time of explosion, which is a direct consequence of the progenitor mass-loss history. Consequently, the mechanisms driving the mass-loss events and their efficiency during the late evolutionary stages are key parameters in determining the classification of the resulting transient (see Heger et al. 2003). Type Ib/c SNe are also labelled as 'stripped envelopes' (Clocchiatti et al. 1996) since their spectra lack H lines, with the Ib and Ic classes being characterised by the presence or absence of strong helium features, respectively (e.g. Filippenko 1997; Shivvers et al. 2019). Specific mass-loss mechanisms are required to efficiently remove the outer layers of progenitor stars thereby leading to stripped envelope SNe. Candidate progenitors include massive Wolf–Rayet (WR) stars and, more predominantly according to observed fractions (Smith et al. 2011), lower mass helium stars stripped in binaries via Roche-lobe overflow or common-envelope evolution. As for the more common Type IIn SNe, emission lines with relatively narrow profiles – i.e. full-width-at-half-maximum (FWHM) velocities of approximately 10^{3} km s^{-1} – are key features in classifying SNe Ibn (Pastorello et al. 2008; Hosseinzadeh et al. 2017, 2019), where the lowercase suffix stands for 'narrow'. Although narrow lines are historically associated with the ongoing dynamical interaction between SN ejecta and the circumstellar medium (CSM), Tartaglia et al. (2025) recently showed that they are not necessarily linked to this mechanism and that their presence may simply act as a probe of a dense, pre-existing gas. They also highlighted how, in at least a fraction of narrow-lined SNe, these may not be related to energy sources in addition to canonical recombination and radioactive decays. A handful of SNe Ibn with well-sampled spectroscopic evolution showed evidence of high-ionisation features (typically He II, C III/IV and N III; see Pastorello et al. 2015a; Gangopadhyay et al. 2020, 2022; Pursiainen et al. 2023; Wang et al. 2024) in their early spectra, but their number is likely affected by the limited number of sufficiently early spectroscopic observations. These are frequently interpreted as signatures of 'flash ionisation' produced by the shock breakout radiation field (Gal-Yam et al. 2014; Groh 2014; Bruch et al. 2023). The Bowen fluorescence mechanism is likely responsible for at least the prominent N III λ4100 and $\lambda\lambda$4634; 4641 features are often observed in these transients (see Selvelli et al. 2007), providing a more physically rigorous framework for the excitation of these specific lines.

The physical origin and progenitor nature of SNe Ibn have been further explored by recent radiation-hydrodynamics and radiative-transfer simulations. Dessart et al. (2022) showed that persistent narrow lines and modest peak luminosities in some

⋆ Corresponding author: leonardo.tartaglia@inaf.it

Open Access article, published by EDP Sciences, under the terms of the Creative Commons Attribution License (https://creativecommons.org/licenses/by/4.0), which permits unrestricted use, distribution, and reproduction in any medium, provided the original work is properly cited.
This article is published in open access under the Subscribe to Open model. Subscribe to A&A to support open access publication.

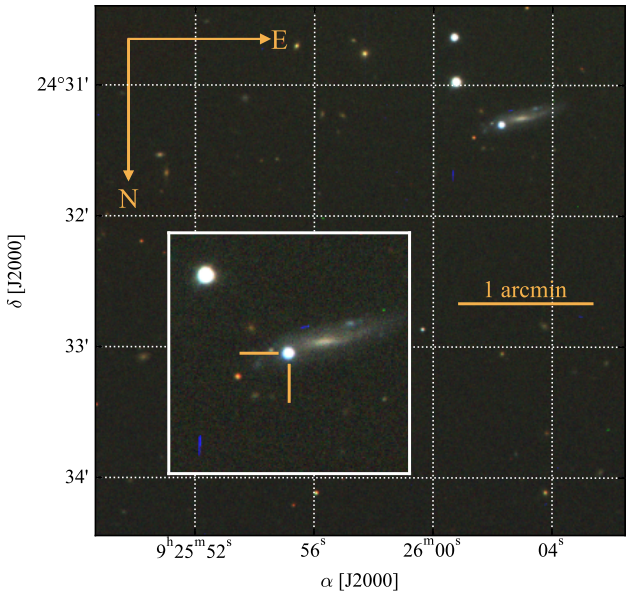


Fig. 1. Colour image of SN 2020able and its host galaxy, obtained by combining *g*-, *r*-, and *i*-band data obtained on 2021 January 21 with the 2.0 m Liverpool Telescope. The transient is the bright source in the middle of the inset.

SNe Ibn are inconsistent with the standard explosion of a massive WR star into a dense wind, suggesting that these events may also arise from low-energy explosions of lower mass helium stars ($\leq 5 M_\odot$) in interacting binary systems. In this scenario, the ejecta collide with a massive, He-rich CSM shell previously ejected through binary interaction or a non-terminal nuclear flash. Notably, their simulations show that the late-time spectra of prototypical Type Ibn SNe such as SN 2006jc and SN 2011hw are dominated by a forest of Fe II emission lines below 5500 Å, producing the hot pseudo-continuum frequently observed in interacting SNe.

In this context, early high-cadence monitoring is crucial to constrain the CSM geometry and test progenitor models. Thanks to a dense observational cadence starting shortly after the explosion, the Type Ibn SN 2020able represents one of the most comprehensively monitored Type Ibn SNe to date, providing the opportunity to clearly trace the transition from an early, geometrically confined ejecta–CSM interaction to the later ejecta-dominated expansion within a highly stratified environment. The discovery of SN 2020able was first reported (Tonry et al. 2020) by the Asteroid Terrestrial-impact Last Alert System (Smith et al. 2020, ATLAS;) in 2020 December 2.54 UT (MJD = 59185.54) with an orange magnitude of approximately 18.9 mag, which assigned the internal name ATLAS20bgkn to the transient. The SN was also observed by the Panoramic Survey Telescope & Rapid Response System (Pan-STARRS Chambers et al. 2016, internal name PS20mdd) and the Zwicky Transient Facility (ZTF; Graham et al. 2019; Bellm et al. 2019; Masci et al. 2019) as ZTF20aayxldg and classified as a Type Ibn SN by Hiramatsu et al. (2020) based on its spectroscopic similarities with SN 2019uo (Gangopadhyay et al. 2020). In Sect. 2, we analyse the local environment within the host galaxy SDSS J092602.93+243115.1 (Sect. 2.1). We then discuss the ultraviolet (UV) and optical light curves and how we modelled their evolution with the Modular Open-Source Fitter for Transients (MOSFiT) package (Sect. 2.2), and we examine the evolution of the main features observed in the optical spectra (Sect. 2.3). Section 3 summarises the main results of our analysis. Data reduction techniques are described in Appendix A, with a log of spectroscopic observations reported in Table A.1.

2. Analysis and discussion

2.1. The local environment

SN 2020able exploded at RA =141°.50943, Dec = +24°.52169 [J2000], −9″.31 E +3″.14N offset from the centre of its host, SDSS J092602.93+243115.1[1] (also known as PGC 1709306 and WISEA J092602.94+243114.9; see Fig. 1). Following Hakobyan et al. (2009), we computed the galactocentric de-projected distance of SN 2020able adopting the host's geometrical parameters reported in the literature. For an inclination of $i = 90°$, position angle of P.A. = 104°.9, and the coordinates of the SN and the host centre, we inferred a de-projected galactocentric distance 10″.70. Fixsen et al. (1996) reported a recessional velocity with respect to the 3K cosmic microwave background of $7695 \pm 20\,\mathrm{km\,s^{-1}}$, and we therefore used this value to estimate a luminosity distance of $D_L = 107.6 \pm 7.4$ Mpc ($\mu = 35.16 \pm 0.15$ mag) assuming a standard cosmology with $\Omega_\Lambda = 0.73$, $\Omega_M = 0.27$ and $H_0 = 73\,\mathrm{km\,s^{-1}\,Mpc^{-1}}$. This choice was made on the basis of cosmologies adopted in the literature and to facilitate comparisons with other Type Ibn SNe (e.g. Pastorello et al. 2016; Hosseinzadeh et al. 2019).

An optical spectrum of the host nucleus was obtained as part of the legacy programme of the Sloan Digital Sky Survey (SDSS; Plate = 2291, FiberID = 39, MJD = 53714; York et al. 2000). We retrieved the flux-calibrated data from SDSS Data Release 12 (DR12; Alam et al. 2015) and estimated the host metallicity using standard diagnostic line ratios. Specifically, we used the re-calibration of the O3N2 (Alloin et al. 1979) and N2 (Denicoló et al. 2002) abundance indicators provided by Marino et al. (2013). The O3N2 indicator in particular is based on the measured line ratios [O III]λ5007/Hβ and Hα/[N II]λ6583 and is therefore less sensitive to extinction given the small wavelength differences between the emission lines involved. Both indicators already give oxygen abundances for the host centre significantly below the solar value (8.35 ± 0.02 dex and 8.40 ± 0.04 dex for O3N2 and N2, respectively, against a typical solar value ≃8.69 dex; see Asplund et al. 2009). The oxygen abundance at the galactocentric distance of SN 2020able is expected to be even lower, following the metallicity gradient of $-0.078 \pm 0.040\,\mathrm{dex\,r_e^{-1}}$ found by Galbany et al. (2016) for SNe Ib/c hosts. The disc effective radius, $r_e = 9''.4 \pm 2''.4$, was derived directly from the definitions of the mean B-band surface brightness and total B-band magnitude (Paturel et al. 1997, 2000) using the values $\mu_{B,e} = 23.99 \pm 0.22\,\mathrm{mag\,arcsec^{-2}}$ and $b_t = 17.14 \pm 0.50$ mag retrieved from HyperLEDA[2]. This yields an abundance of 12 + log(O/H) = 8.28 ± 0.03 dex, calculated as the weighted average of the values derived using the O3N2 (8.35 ± 0.02) and N2 (8.40 ± 0.04 dex) diagnostics.

The foreground Galactic reddening towards SN 2020able is $E(B-V) = 0.028$ mag (Schlafly & Finkbeiner 2011), while the contribution of the local environment was derived using empirical relations between the colour excess and equivalent widths (EWs) of Na ID lines, as detailed in Poznanski et al. (2012). Na ID features were resolved in our spectra obtained with the 6.5 m MMT in 2020 December 13, 2021 January 5, and 2021 February 4 (≃13, 35, and 64 days after the estimated explosion

[1] As reported at https://ned.ipac.caltech.edu
[2] http://atlas.obs-hp.fr/

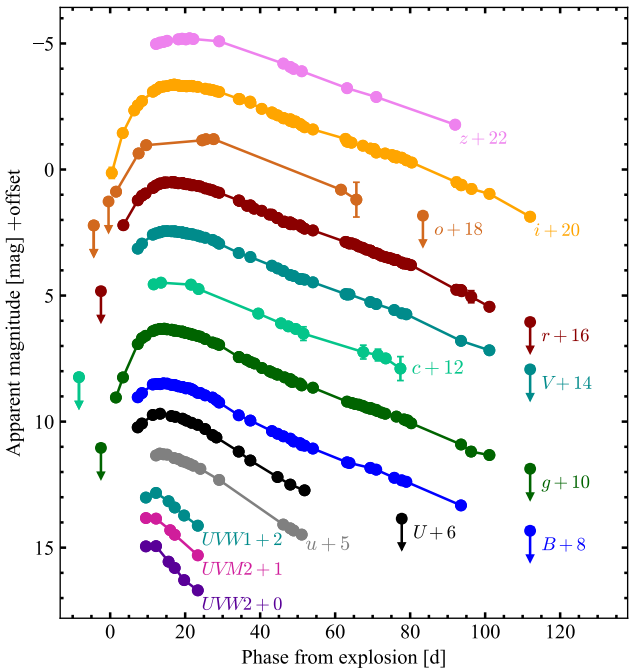


Fig. 2. UV/optical light curves of SN 2020able. Rest-frame phases refer to the explosion epoch estimated through the last non-detection limit. Magnitudes were not corrected for reddening along the line of sight.

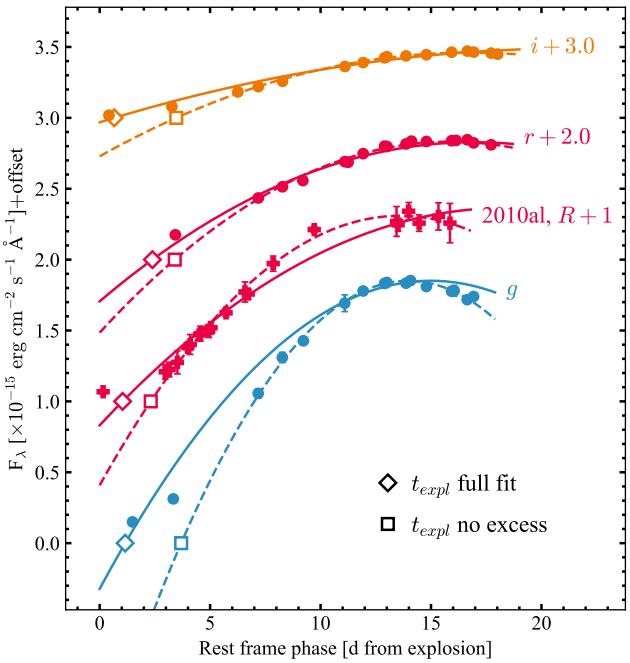


Fig. 3. Early evolution of *gri* light curves of SN 2020able and the *R*-band light curve of SN 2010al, along with a t^2 fit to the derived fluxes. To highlight the early excess, we also show the best fit obtained removing the first one or two points. When extrapolating the flux to zero, both yield explosion dates that occurred after the SN discovery (reported using open squares and diamonds).

epoch; see Sect. 2.2). We took the EWs measured from the first spectrum – the one with the highest signal-to-noise ratio – resulting in 0.26 and 0.18Å for the D2 and D1 lines, respectively. Using a weighted average of Eqs. (7) and (8) of Poznanski et al. (2012), these correspond to an additional contribution of $E(B-V) = 0.046 \pm 0.012$ mag to the total reddening. The colour excess derived from the Na ID Galactic features visible in the same spectrum is in agreement with that reported by Schlafly & Finkbeiner (2011) for the Milky Way reddening contribution and also suggests $E(B-V)_{host} \gtrsim 0.03$ mag comparing the strength of the two sets of features. In the following, we therefore use $E(B-V) = 0.074 \pm 0.012$ mag for the total reddening along the line of sight of SN 2020able.

2.2. Photometry

The UV to optical light curves of SN 2020able are shown in Fig. 2. Details on the instrumentation used and data reduction are provided in Appendix A.

From the analysis of public ZTF data, we identified *gri* prediscovery detections as early as 2020 December 1.39 UT (JD = 2459184.89), approximately 1.15 days before the reported discovery. The last non-detection, on the other hand, was obtained just 0.86 days earlier by the ATLAS survey (JD = 2459184.03, $o > 19.3$ mag) and provides a more stringent constraint on the explosion epoch of SN 2020able. In the following, we thus adopt JD = 2459184.46 ± 0.43 (the midpoint between the ATLAS non-detection and the first ZTF detection) as the explosion epoch and refer all subsequent temporal phases to this date. Forced photometry on ZTF and ATLAS archival frames did not reveal additional detections, ruling out pre-explosion outbursts down to an average *g*- and *r*-band absolute magnitude of −13.7 mag in the approximately two years before the SN explosion.

The early photometric evolution is relatively slow compared to that of other SNe Ibn. A polynomial fit to the UV bands resulted in rise times of 10.6, 10.4, and 11.7 days (in the rest-frame) for the *UVW2*-, *UVM2*-, and *UVW1*-bands, respectively, although the lack of coverage at $t \lesssim +9$ days suggests that a more rapid rise to maximum cannot be definitively ruled out. More robust estimates were derived for the optical bands, where data were available soon after discovery, confirming the relatively slow early evolution, with rise times ranging from approximately 13.3 to 17.0 days in the *u*/*U*- and *z*-bands, respectively. We obtained similar rise times by fitting a t^2 power law (see e.g. Arnett 1982; Riess et al. 1999, and references therein) to the rising parts of the *gri* light curves (the best sampled around the peaks; see Fig. 3), with $t_{rise} \simeq 14.0$, 15.9, and 16.8 days in the *g*, *r*, and *i* bands, respectively. Interestingly, we note a deviation from the t^2 evolution at $t \lesssim +5$ days, with an excess in the derived flux relative to that expected by the 'fireball' model.

To investigate potential similarities among SN 2020able and other Type Ibn/Icn SNe, we selected a comparison sample (see Appendix B) based on the quality of their early light-curve coverage, prioritising events with the best-sampled *r*/*R*-band light curves during the rising phase. In the few cases where these bands were unavailable or lacked sufficient early-time data, other optical bands were considered. In Fig. 4, we plot their peak magnitudes against their respective rise times, computed by fitting a second-order polynomial to the light curve. For each transient, we estimated the explosion and maximum light epochs with the corresponding absolute peak magnitude by performing 10^4 Monte Carlo simulations randomly shifting each data point within its uncertainty. t_{expl}, t_{max}, m_{abs}, and their respective errors (see Appendix B) are the mean values and standard deviations of the resulting distributions. Absolute magnitudes were computed using the most recent redshift-independent distance to each transient or the host redshift, assuming a standard cosmology with $\Omega_\Lambda = 0.73$, $\Omega_M = 0.27$ and $H_0 = 73$ km s^{-1} Mpc^{-1}. For

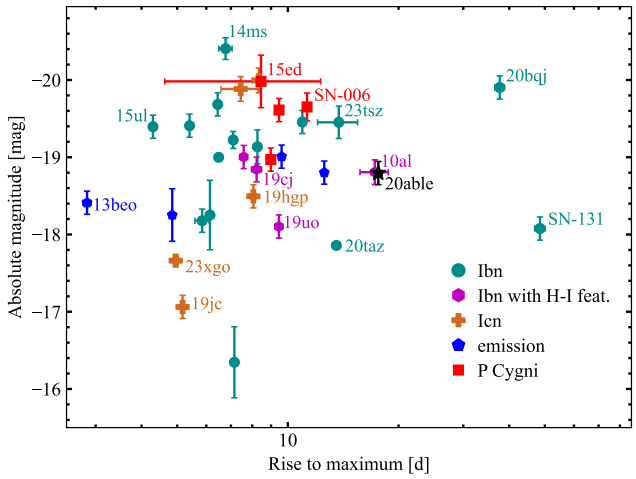


Fig. 4. Absolute peak magnitudes versus rise times for a sample of Type Ibn/Icn SNe with well-sampled early light curves. Ibn subtypes are those reported by Hosseinzadeh et al. (2017). Data points and the corresponding literature references for the light curves used to generate this figure are provided in Table B.1.

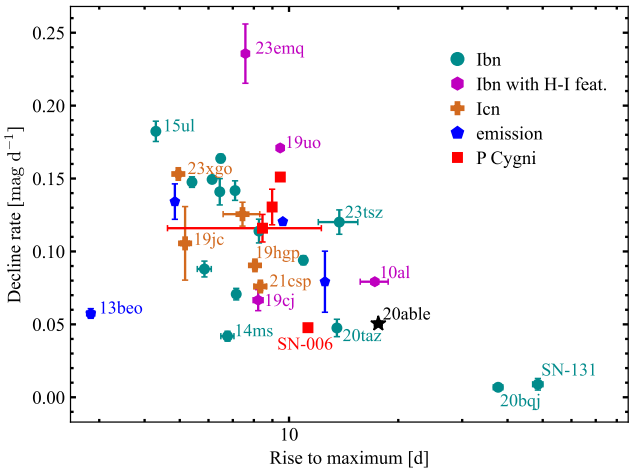


Fig. 5. Decline rates versus rise times for the sample of Fig. 4. Data points used to generate this figure are provided in Table B.1.

SNe 2010al and 2020able, we considered the explosion epochs constrained by the pre-discovery non-detection limits (see Pastorello et al. 2015a, and above) based on their peculiar early photometric evolution (see Fig. 3). The resulting rise times for SNe 2010al and 2020able are, on average, approximately 54% longer than the mean value of the full sample and 92% longer without considering the exceptionally long ones: SNe 2020bqj and OGLE-2014-SN-131 (Kool et al. 2021; Karamehmetoglu et al. 2017). In particular, Type Ibn SNe showing high-ionisation features in their early spectra have a systematically faster evolution with respect to SN 2020able, with the exception of SN 2010al. Following the same procedure, we measured the post-peak decline rates of the entire sample up to 20 days from the maximum light. This yielded a remarkably slow decline rate of approximately 0.05 mag days^{-1} for SN 2020able, close to the slow-evolving behaviour inferred for iPTF13beo, ASASSN-14ms, 2020taz, OGLE-2014-SN-131, OGLE-2012-SN-006, and 2020bqj (see Fig. 5). Specifically, SN 2020able exhibits a post-peak decay slower than 84.4% of the full sample (81.5% limiting the comparison to SN Ibn).

As already suggested by the comparison in Fig. 4, SN 2010al is the only transient showing an early evolution similar to that of SN 2020able, with a comparable rise to the maximum and early spectroscopic evolution. SN 2010al also showed an early excess in its early R-band light curve similar to the one observed in SN 2020able (see Fig. 3), suggesting a common mechanism responsible for the extra luminosity output. To further explore these similarities and their physical meaning, we modelled the UV to optical light curves of SNe 2010al and 2020able with the MOSFiT[3] (Guillochon et al. 2018) tool. Given the rapid photometric evolution of both transients, we initially adopted a non-interacting model, which accounts for the evolution solely through the ^{56}Ni to ^{56}Co radioactive decay (the DEFAULT model in MOSFiT; Nadyozhin 1994). This model fails to reproduce the light curves of both SNe 2010al and 2020able without invoking unphysical nickel masses (specifically, $M_{^{56}Ni} \gtrsim M_{ej}$; see Table C.1). The most significant discrepancy between the models and the observed light curves occurs around the peak, particularly within the UV bands (Table C.1 and Fig. C.1). We therefore used the CSMNI analytical model, which combines the contribution of interaction between the SN ejecta and a dense CSM (e.g. Chatzopoulos et al. 2013; Villar et al. 2017; Jiang et al. 2020) and the luminosity produced by radioactive decays (e.g. Arnett 1980; Nadyozhin 1994). The parameter space was explored using the dynamic nested sampling algorithm DYNESTY (Speagle 2020), to ensure robust convergence of the posterior distributions, allowing MOSFiT to run until the default convergence criterion[4]. Flat priors were used for all parameters. To minimise the number of free parameters, we considered a gamma-ray opacity $\kappa_\gamma = 0.03\,\mathrm{cm^2\,g^{-1}}$ (typical for a He-rich medium; Morozova et al. 2015) and SN ejecta with a constant inner density profile ($\delta = 0$). Although a standard radiative envelope for a pure WR progenitor suggests an outer ejecta-profile index of $n \simeq 10$, adopting this value in our modelling severely underestimates the host-galaxy extinction derived from the Na ID features. As discussed by Matzner & McKee (1999), deviations towards shallower ejecta profiles ($n \simeq 7$) are expected for stripped-envelope progenitors that experienced violent pre-explosion mass loss (see e.g. the case of SN 1993J; Nomoto et al. 1995). We therefore let n vary within reasonable values for stars with radiative envelopes (i.e. 6–10). The radius at which the transition from $\rho \propto r^{-\delta}$ to r^{-n} occurs in the density profile of the ejecta is defined by the dimensionless radius $x_0 = r_0(t)/R_{SN}(t)$, where the density evolves as $\rho_{SN} = g^n\, t^{n-3}\, r^{-n}$. The normalisation constant $g^n = 1/(4\pi(\delta - n))[2(5-\delta)(n-5)E_k]^{(n-3)/2}/[(3-\delta)(n-3)M_{ej}]^{(n-5)/2}$ depends on the total ejected mass, M_{ej}, the total SN kinetic energy, E_k, and the assumed power-law indices n and δ (see Chevalier & Fransson 1994). Within this framework, MOSFiT determines the transition radius, r_0, to ensure that the ejecta density profile remains physically consistent with the main explosion parameters. We also assumed a CSM with a density profile of $\rho \propto r^{-2}$ (the 'wind scenario'). We note that although Maeda & Moriya (2022) invoked a steeper density profile ($\propto r^{-3}$) to reproduce the rapid post-peak decay typically observed in SNe Ibn, such a steep density gradient is observationally incompatible with the slow post-peak evolution of SN 2020able. Consequently, whilst the standard wind-like profile ($s = 2$) is dictated by the

[3] https://github.com/guillochon/MOSFiT

[4] As discussed in https://mosfit.readthedocs.io/en/latest/fitting.html

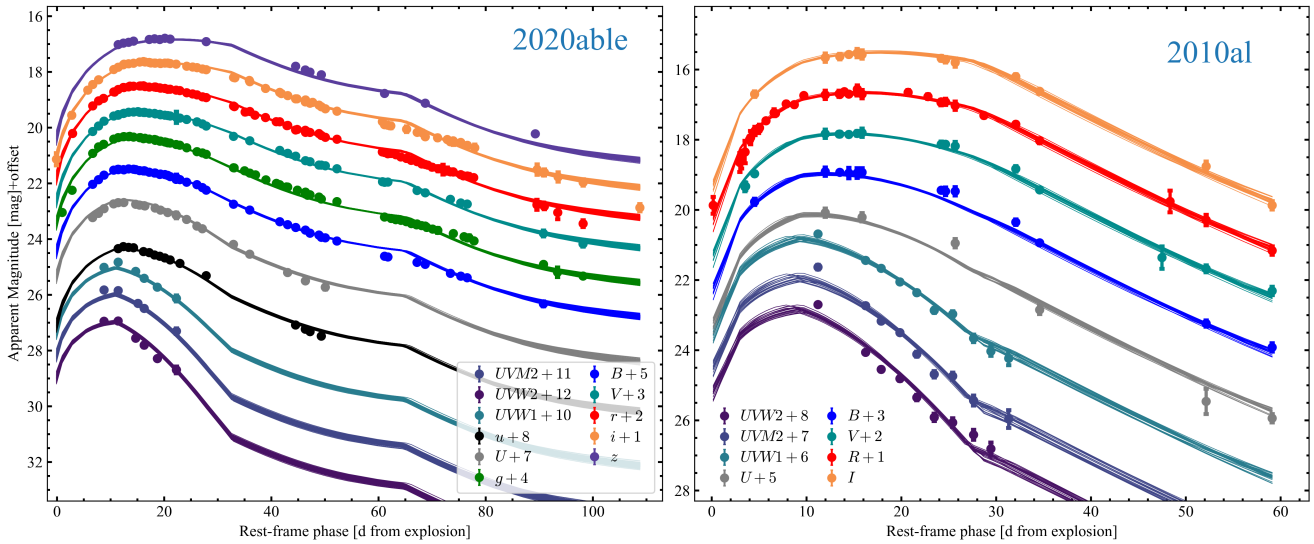


Fig. 6. Multi-band light curves of SNe 2020able and 2010al along with an ensemble of models generated by MOSFiT. Light curves have been vertically displaced by the indicated offsets. Rest-frame phases refer to the estimated explosion epoch.

native limitations of MOSFiT (which requires $s \leq 2$), it remains observationally well justified by the slow evolution of the transient. To further test the efficiency of interaction, we explored a pure CSM model for both transients. For SN 2020able, we also used the spectroscopic velocity and host extinction estimates derived for SN 2020able, fixing $v_{\rm ej} = 5.5 \times 10^3$ km s^{-1} and matching the late-time broad He I lines at +98 days and $N_{\rm H} = 3.1 \times 10^{20}$ cm^{-2}, based on the Na ID equivalent widths. All models converged successfully for both objects (see Figs. 6, C.2, and C.3), but revealed distinct physical configurations despite their photometric similarities (see Tables C.2 and C.3). Although both events exhibit sub-canonical kinetic energies ($E_{\rm k} \simeq 2.9 \times 10^{50}$ erg for SN 2020able and 3.8×10^{50} erg for SN 2010al) and high temperature floors ($T_{\rm min} \simeq 7500$–7700 K), consistent with the helium recombination temperature (e.g. Dessart et al. 2020), their power sources and ejecta properties diverge significantly. For SN 2020able, the best-fit CSMNI model yields an ejected mass of $M_{\rm ej} \simeq 1.3\,{\rm M}_\odot$, a circumstellar shell mass of $M_{\rm CSM} \simeq 0.6\,{\rm M}_\odot$ located at an inner radius of $R_0 \simeq 0.3$ AU ($\simeq 64\,{\rm R}_\odot$), and a synthesised nickel mass of $M_{^{56}{\rm Ni}} \simeq 3.2 \times 10^{-2}\,{\rm M}_\odot$. We note that both R_0 and $\rho_{\rm csm}$ exhibit broad posterior distributions spanning over an order of magnitude (see Figs. C.2 and C.3), a known manifestation of parameter degeneracies among shell location, density, and interaction efficiency in light-curve modelling. However, even considering the 16th–84th percentile confidence intervals ($R_0 \simeq 0.1$–0.6 AU), the inner boundary remains strictly constrained within $\lesssim 1$ AU, preserving a compact circumstellar environment. In contrast, for SN 2010al, the CSMNI fit indicates a negligible nickel contribution ($M_{^{56}{\rm Ni}} \simeq 6.5 \times 10^{-3}\,{\rm M}_\odot$), suggesting that its light curve is largely dominated by ejecta–CSM interaction. Indeed, a pure CSM model for SN 2010al provides a viable alternative but requires a substantially more massive shell ($M_{\rm CSM} \simeq 2.64\,{\rm M}_\odot$) extending up to $R_0 \simeq 6.9$ AU. For SN 2020able, the CSM model can mathematically fit the light curve, but it forces the inner boundary of the shell to an unrealistically large radius of $R_0 \simeq 35.5$ AU with an extremely low density ($\rho_{\rm csm} \simeq 5.6 \times 10^{-13}$ g cm^{-3}).

Differences in the preferred model can be physically linked to their different post-peak light-curve decline rates and the intrinsic limitations of the MOSFiT code. As highlighted by Maeda & Moriya (2022), fast-evolving Type Ibn SNe such as SN 2010al require a steeper CSM density profile ($\rho \propto r^{-s}$ with $s \simeq 3$) to account for their rapid post-peak declines while maintaining physically realistic explosion and CSM parameters. Since MOSFiT natively requires $s \leq 2$, it cannot easily fit rapidly declining transients without artificially boosting $M_{\rm CSM}$ or reducing $M_{^{56}{\rm Ni}}$. Conversely, SN 2020able displays a remarkably slower post-peak evolution, making the standard wind-like profile ($s = 2$) both mathematically suitable and observationally well-justified. Interestingly, for SN 2010al all models require a non-negligible host reddening, in contrast to the value reported in the literature, with the CSM model suggesting a neutral hydrogen column density of $N_{\rm H} = (9.1 \pm 0.65) \times 10^{20}$ cm^{-2} (corresponding to $A_V = 0.412 \pm 0.034$ mag, according to Güver & Özel 2009). To further explore this discrepancy, we checked the mid-resolution X-shooter spectra of SN 2010al published by Pastorello et al. (2011). Specifically, we estimated the host contribution to the total reddening by measuring Na ID EWs in spectra obtained around maximum light and approximately two months after explosion (see Sect. 2.1), and the derived values were roughly in agreement with that predicted by MOSFiT at both phases (0.60 ± 0.16 mag, averaging Eqs. (7) and (8) in Poznanski et al. 2012).

Despite the modest CSM masses derived from the modelling, both transients reached high peak luminosities, indicating efficient conversion of kinetic energy into radiation. The high recombination temperatures confirm stripped-envelope progenitors for both events, but the significantly larger synthesised ^{56}Ni mass in SN 2020able points towards a more massive and compact progenitor star. Combined with the CSM expansion velocities inferred from the spectral lines (Sect. 2.3), this evidence supports SN 2020able having a Wolf–Rayet progenitor (e.g. Crowther 2007).

The temporal evolution of the photospheric properties of SN 2020able was estimated by constructing the spectral energy distributions (SEDs) from multi-band photometry. To ensure consistent sampling, light curves were linearly interpolated to the epochs of the r-band observations, with a baseline tied to the earliest Swift/UV data to capture the UV flux that dominates the early SED of core-collapse SNe (e.g. Tomasella et al. 2013). Sequential blackbody fits yielded a peak bolometric luminosity of $L_{\rm peak} \simeq 4.4 \times 10^{43}$ erg s^{-1} (see Fig. 7

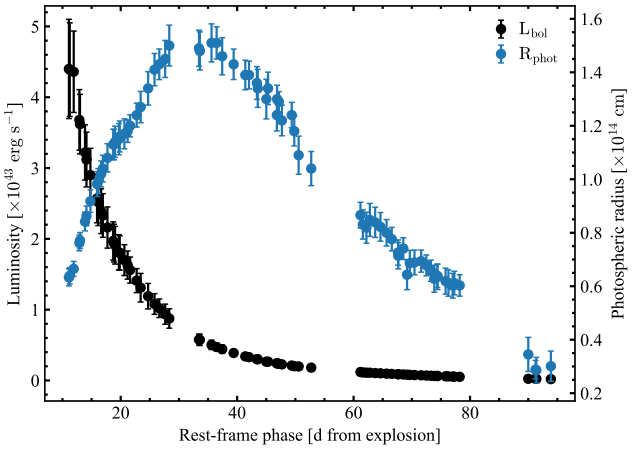


Fig. 7. Evolution of photospheric radius and the bolometric luminosity as derived by fitting a blackbody to the SED of SN 2020able. Rest-frame phases refer to the estimated explosion epoch.

and Table 1). At +11 days, the photosphere remains hot ($T_{\rm ph} \simeq 2.0 \times 10^4$ K), approximately 35% higher than estimated from the optical continuum alone, underscoring the need for UV coverage in interacting transients. Conversely, the derived temperatures and photospheric radii vary rapidly, arguing against interaction significantly shaping the overall evolution. The rapid decline of the light curves at later phases, along with the observed spectroscopic evolution (see Sect. 2.3), also highlight a 'mild' interaction scenario. In this framework, interaction contributes to the transient luminosity but remains secondary to the dynamics of the underlying ejecta at later phases, consistently with the evolution of fast-evolving SNe Ibn (e.g. Pastorello et al. 2015a, 2016). This interpretation is also supported by the observed spectroscopic evolution (see Sect. 2.3) as well as the agreement between the photospheric radius obtained from SED fitting and the physical parameters estimated with MOSFiT, which also explain the early *gri*-band excess (see Fig. 3). Given the best-fit CSMNI average density of $\rho \simeq 9.3 \times 10^{-9}$ g cm^{-3} and $M_{\rm CSM} \simeq 0.6\,{\rm M}_\odot$, we infer an outer radius for the interacting shell of approximately 3.1×10^{13} cm (assuming an inner radius $R_0 \simeq 3.7 \times 10^{12}$ cm; see Table C.2). This indicates a remarkably compact interaction region ($\Delta R \simeq 2.7 \times 10^{13}$ cm) that is rapidly swept up by the expanding SN ejecta. In this picture, the interaction is confined both spatially ($\lesssim 3 \times 10^{13}$ cm) and temporally (within the first few days post-explosion), reinforcing that the late-time behaviour of SN 2020able is likely dominated by the expanding ejecta rather than ongoing interaction.

2.3. Spectroscopy

Optical spectra are shown in Figs. 8, 9, and 10, while details of the instruments used to carry out the follow-up campaign, reduction steps, and a log of the spectroscopic observations are reported in Appendix A. Early spectra showed a hot continuum rapidly decreasing from $\simeq 2.0 \times 10^4$ to $\simeq 1.4 \times 10^4$ K within the first 16 days after the explosion, as estimated by fitting a blackbody to the spectral continuum after excluding regions dominated by strong emission features. Prominent C III, N III, He II, and He I lines, often visible during the early phases of CC SNe, were clearly detected within the same period. In Type Ibn SNe with similar early features (e.g. SNe 2010al, 2019cj, 2019uo, 2019wep, and 2023emq; see Fig. 4 and Table B.1), these typically last longer than in hydrogen-rich SNe before disappearing below

Table 1. Photospheric parameters obtained fitting a blackbody to the SED of SN 2020able using UV and optical data.

Phase	$T_{\rm ph}$ (err)	$R_{\rm phot}$ (err)	$L_{\rm bol}$ (err)
(d)	(K)	$\times 10^{14}$ cm	$\times 10^{43}$ erg s^{-1}
+11	19817(610)	6.33(0.32)	4.40(0.70)
+11	19710(573)	6.39(0.31)	4.39(0.66)
+12	19292(491)	6.65(0.28)	4.36(0.58)
+13	17265(375)	7.62(0.30)	3.68(0.43)
+13	17101(370)	7.71(0.30)	3.62(0.42)
+14	15889(350)	8.42(0.35)	3.22(0.39)

Notes. Rest-frame phases are relative to the estimated explosion epoch. The table is published in its entirety in a machine-readable format, available at the CDS. A portion is shown here for guidance regarding its shape and content.

the continuum level. We identified relatively narrow (FWHM velocity $\simeq 3 \times 10^3$ km s^{-1}) He I λ3889, 5876, and 6678 lines, along with prominent C III λ5696, N III λ4634–4641 (multiplet 2; see Moore 1945) and λ4100, and He II λ4686. N III λ4100 is likely formed by the blend of the $\lambda\lambda$4097, 4103 doublet (see Walborn 1972, and Fig. 9). This is the only high-ionisation line with an absorption component, corresponding to an expansion velocity of $\simeq 1.3 \times 10^3$ km s^{-1}, which is comparable to those measured from the P Cygni absorption minima of the He I lines (see the inset in Fig. 8). High-ionisation features were clearly visible up to +14 days, while we only tentatively identified a shallow emission corresponding to C III λ5696 at +14 and +16 days. Tartaglia et al. (2025) showed that the N III lines in the early spectra of SN 2024bch were likely produced by the Bowen fluorescence mechanism. This is triggered by the near-coincidence of He II Ly-α λ303.783 and O III λ303.799, followed by a second resonance between O III λ374.436 and N III $\lambda\lambda$374.434, 374.441 (see e.g. Selvelli et al. 2007). In this framework, He II λ4686 and C IV λ5696 emerge from the subsequent recombination cascades of He and C. This interpretation may also apply to SN 2020able, given the high temperatures inferred from its spectral continuum up to +16 days. Indeed, these estimates should be regarded as conservative lower limits, since the SED peak falls at wavelengths significantly shorter than those covered by our optical spectra (see Sect. 2.2, where we estimate $T_{\rm ph} \simeq 2.0 \times 10^4$ K at +11 days); the actual temperatures are likely higher, further supporting the presence of a high-ionisation regime. Assuming that these features are driven by the Bowen fluorescence mechanism, their prolonged persistence in Type Ibn SNe – compared to hydrogen-rich events – is likely due to the hydrogen-deficient nature of their circumstellar envelopes. This reduces the competition for ionising photons and prevents the absorption of the He II resonance line by neutral hydrogen, thus sustaining the emission more efficiently.

Whereas the main He I lines (λ3889, 5876, and 6678) were unambiguously identified due to the absence of nearby features, our early spectra lacked the resolution to distinguish the individual components of the complex emission around 4670 Å. For the same reason, we cannot rule out the presence of C IV $\lambda\lambda$5801, 5812 (typically observed along with C III λ5696 and C IV λ4658 in the spectra of WR stars; Crowther et al. 1998), which may be blended with C III λ5696 and He I λ5876. We therefore compared our +7 days spectrum with the much higher resolution one of SN 1998S obtained approximately five days after explosion in the same spectral region (see Fig. 9). Beyond the Balmer

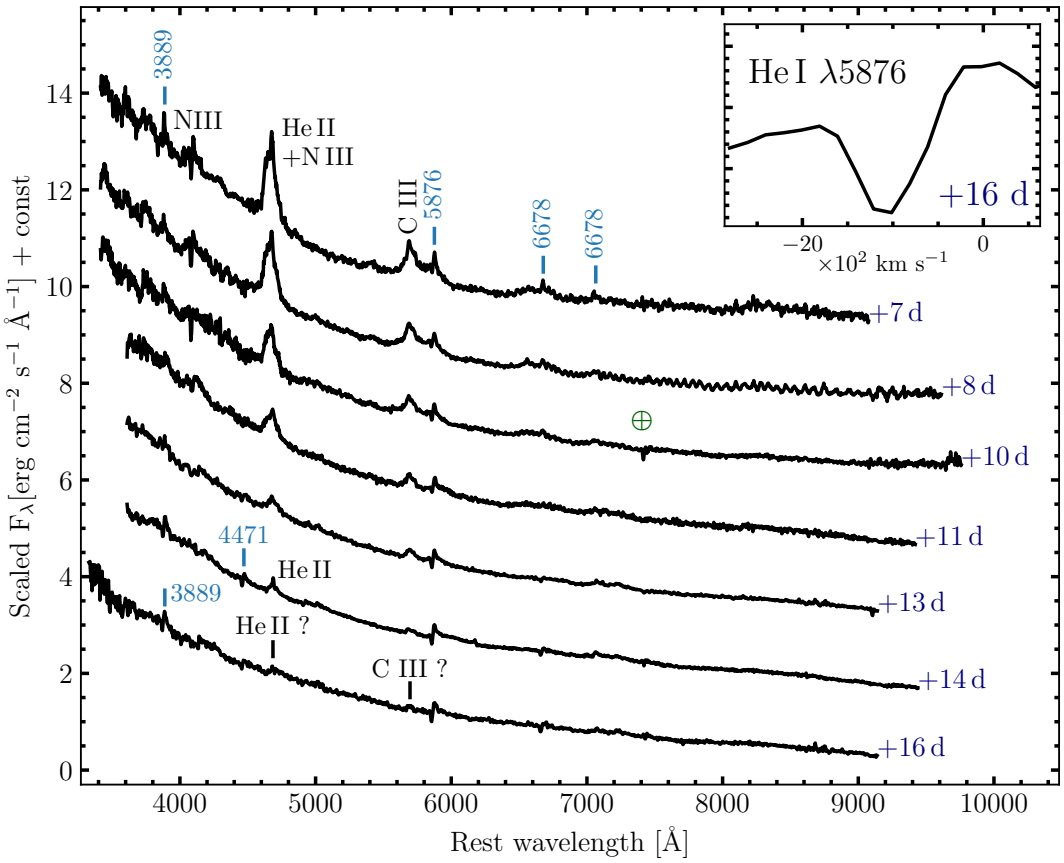


Fig. 8. Early spectroscopic evolution of SN 2020able at $t < +16$ days along with a line identification of the main emission features. He I lines are reported with their corresponding rest wavelengths. The ⊕ symbol marks the position of the O_2 telluric feature (Band A) around 7500 Å. The inset shows a zoomed-in view of He I λ5876 at +16 days in the velocity plane. Rest-frame phases refer to the estimated explosion epoch.

lines, consistent with its classification as a hydrogen-rich CC SN, SN 1998S exhibited both N III λ4097 and λ4103. These features displayed narrow P Cygni profiles, indicating expansion velocities of $\simeq$20 km s^{-1}, notably lower than the $\simeq 1.3 \times 10^3$ km s^{-1} observed in SN 2020able, highlighting the remarkable disparity in velocities of the absorbing shells. As in SN 2020able, the N III λ4100 doublet is the only high-ionisation line clearly showing an absorption component, while N III $\lambda\lambda$4634, 4641, C IV λ4647–4651, and He II λ4686 are purely in emission. Although the resolution of our +7 days spectrum does not allow us to identify all these features, we cannot rule out their presence in the early spectra of SN 2020able. A resolution of $R \gtrsim 4000$ is therefore crucial in order to fully identify spectroscopic features in the early spectra of interacting transients such as Type Ibn SNe.

In Fig. 9, we also show a tentative fit to the main features within the first 11 days from explosion, a period during which all components remain clearly discernible above the spectral continuum. In our fit, we considered the contributions of N III λ4634, He II λ4686, C III λ5696, and He I λ5876 and adopted Lorentzian profiles to follow the shape of the electron-scattering wings. Although we note that such profiles may not be fully captured by a Lorentzian shape, particularly at higher resolutions (Huang & Chevalier 2018; Tartaglia et al. 2020), the overall profiles were well-reproduced assuming a constant FWHM of approximately $\simeq 3 \times 10^3$ km s^{-1} at all times, leaving only the peak wavelengths and line fluxes as free parameters. Interestingly, all emission features have centroids roughly at their corresponding rest wavelengths, with no evidence of efficient radiative acceleration (see e.g. Fransson et al. 2014). This is consistent with the evolution of high-ionisation features observed in SN 2024bch (Tartaglia et al. 2025) and potentially places the emitting shell at a distance where radiative acceleration becomes negligible. This scenario is further supported by the constant FWHM of the emission lines. A compact, nearby shell being swept up by the rapidly expanding SN ejecta would have introduced a shocked component, thus modifying the FWHM within the first 16 days; this was ruled out by our fitting procedure. This points towards a stratified circumstellar environment, likely composed of multiple distinct shells: an inner one contributing to the early interaction and luminous peak, and outer regions responsible for the high-ionisation lines and the persistent narrow He I features observed up to approximately +70 days (see below).

At $t \gtrsim +16$ days, high-ionisation features fade and narrow He I lines with prominent P Cygni profiles are the only features visible above a hot continuum. We identified He I λ3889, λ4471 (appearing already at +14 days), λ4686, and λ5876. All helium lines showed an absorption minimum corresponding to an expansion velocity of approximately 1.2×10^3 km s^{-1} and a blue velocity at zero intensity (BVZI; see e.g. Taddia et al. 2020) of approximately 1.8×10^3 km s^{-1}, which remained constant up to +75 days, after which the absorption component is no longer visible. Within the same period, its EW, measured by a simple Gaussian fit, remained roughly constant until approximately +47 days, when it showed a sudden drop (see Fig. 10). At +43 days, the He I λ5876 profile underwent a significant metamorphosis, displaying a much broader emission accompanied by a blueshifted absorption component. From its minimum, we derived a photospheric velocity of approximately

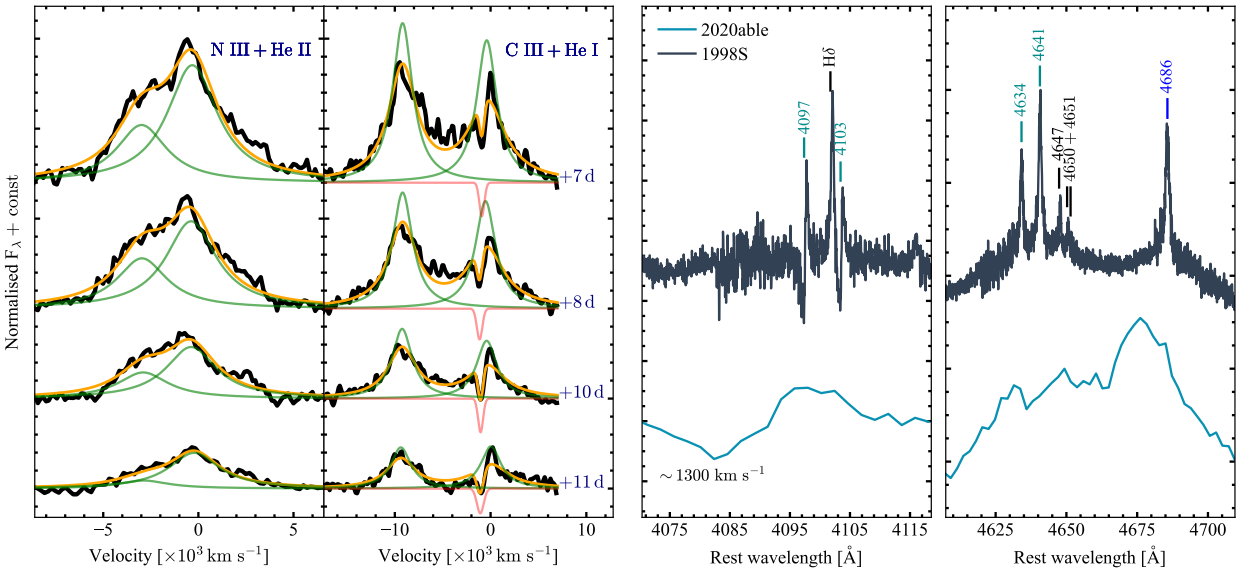


Fig. 9. *Left*: multi-component fit to the N III+He II and C III+He I regions. A Gaussian absorption was used to reproduce the overall profile of He I λ5876. The widths and peaks of the features remain constant throughout the evolution of the high-ionisation feature, with a FWHM$_{vel} \simeq 3.0 \times 10^3$ km s^{-1}. *Right*: comparison of the spectrum obtained at +7 days with the one of SN 1998S, with a much higher resolution, obtained approximately five days after explosion (see Shivvers et al. 2015).

6.7×10^3 km s^{-1}, although the nature of this absorption may be considered ambiguous due to the proximity of Fe II lines (e.g. multiplets 41, 42, 48, 49, and 52; Moore 1945). However, its minimum decreased monotonically to 5.5×10^3 km s^{-1}, as observed at +98 days, which is consistent with a receding photosphere mapping progressively deeper layers of the SN ejecta. At +43 days, we also tentatively identified a distinct absorption consistent with Fe II λ5169, resulting in a velocity of approximately 4.0×10^3 km s^{-1}; this is consistent with the value inferred from the SED fitting (see Sect. 2.2). These results, along with the rapid photometric decline and the monotonically decreasing blackbody radius, collectively suggest that the ejecta–CSM interaction does not contribute to the energetic output of SN 2020able at these phases.

The most straightforward interpretation for the sudden drop in the EW of the narrow He I absorptions at $t \gtrsim +47$ days and their disappearance at $t \gtrsim +70$ days is that the SN ejecta have finally overtaken the circumstellar shell. In this scenario, we can estimate the geometric extent of this He-rich material by adopting the ejecta expansion velocity derived above, which provides a direct constraint on its inner and outer radii. Specifically, if the drop in the EW of the narrow absorption corresponds to the time at which the expanding ejecta reach the inner boundary of the shell, assuming $v_{ej} = 6.7 \times 10^3$ km s^{-1} and a CSM expansion velocity of 1.2×10^3 km s^{-1} would result in an inner radius of $R_{in} \simeq 2.2 \times 10^{15}$ cm. Furthermore, the disappearance of the narrow absorption at approximately +70 days suggests an outer radius of $R_{out} \simeq 3.3 \times 10^{15}$ cm. Alternatively, the absorption components may be diluted in the blue wing of the emerging He I broad emission lines, which dominated the spectra from +43 days (see Fig. 10).

The geometric extent of the shell, combined with the expansion velocity of the bulk material estimated from the minimum of the narrow P Cygni profiles, can be used to constrain the physical properties of the CSM and the mass-loss episode that generated it. Assuming a constant expansion velocity of 1.2×10^3 km s^{-1} and the calculated inner and outer radii, we estimate that the mass-loss episode began approximately 321 days before the SN explosion and ended roughly 216 days before it. Furthermore, He II λ4686 being visible in the early spectra of SN 2020able implies a recombination timescale of $t_{rec} < 7$ days for the He-rich shell, providing a minimum electron density of $n_e > (t_{rec}\alpha_{rec})^{-1}$. Adopting $\alpha_{rec} = 9.08 \times 10^{-13}$ cm^3 s^{-1} (typical for He-rich gas at $T_e = 2.0 \times 10^4$ K; Osterbrock & Ferland 2006), we obtain $n_e > 1.8 \times 10^6$ cm^{-3}. A more stringent constraint for the local density can be derived from the narrow emission lines visible until +16 days. As derived above, their FWHM ($\simeq 3 \times 10^3$ km s^{-1}) remained constant throughout the evolution of the high-ionisation features (see Fig. 9). For line profiles dominated by electron scattering, this width is not indicative of the expansion velocity of the shell (see Huang & Chevalier 2018), which we directly estimated at roughly a third of this value from the absorption minima of the He I and N III lines. The discrepancy is even more relevant for relatively compact shells, where the FWHM probes the Thomson optical depth (τ_{es}) for a given T_e. For $\eta = R_{out}/R_{in} \simeq 1.5$, a FWHM of 3×10^3 km s^{-1} corresponds to $\tau_{es} \simeq 6.0$–7.0 for an electron temperature of $T_e = 2.0 \times 10^4$ K and reasonable density profiles ($\rho \propto r^{-2}$ with $s = 0$, 1 and 2; see Fig. 5 in Huang & Chevalier 2018). This range of τ_{es} is also supported by the overall shape of the emission lines; while the expansion velocity of the shell is expected to produce asymmetric electron-scattering profiles (i.e. with an excess in their red wings), Huang & Chevalier (2018) showed that the combined effects of a thin shell and a high optical depth can still produce the symmetric features observed in SN 2020able even in shells with relatively high expansion velocities. Taking $\tau_{es} = 6.5$, we derive $n_e = \tau_{es}/(\sigma_T \Delta R) \simeq 1.4 \times 10^9$ cm^{-3}, which implies a mass-loss rate of 8.7×10^{-2} M$_\odot$ yr^{-1} assuming a typical filling factor of $f = 0.1$ for a WR wind (see e.g. Flores et al. 2023), a fully ionised helium composition, and an event lasting approximately 105 days. This value is inconsistent with the wind velocity measured from the He I P Cygni minima – which are comparable to those of steady winds in late WN (WN7-8) or very late WC stars (e.g. WC9; see Crowther 2007); however, this suggests that the layer with $\tau_{es} = 6.5$ was generated by a shorter eruptive event similar to the one observed two years prior to the

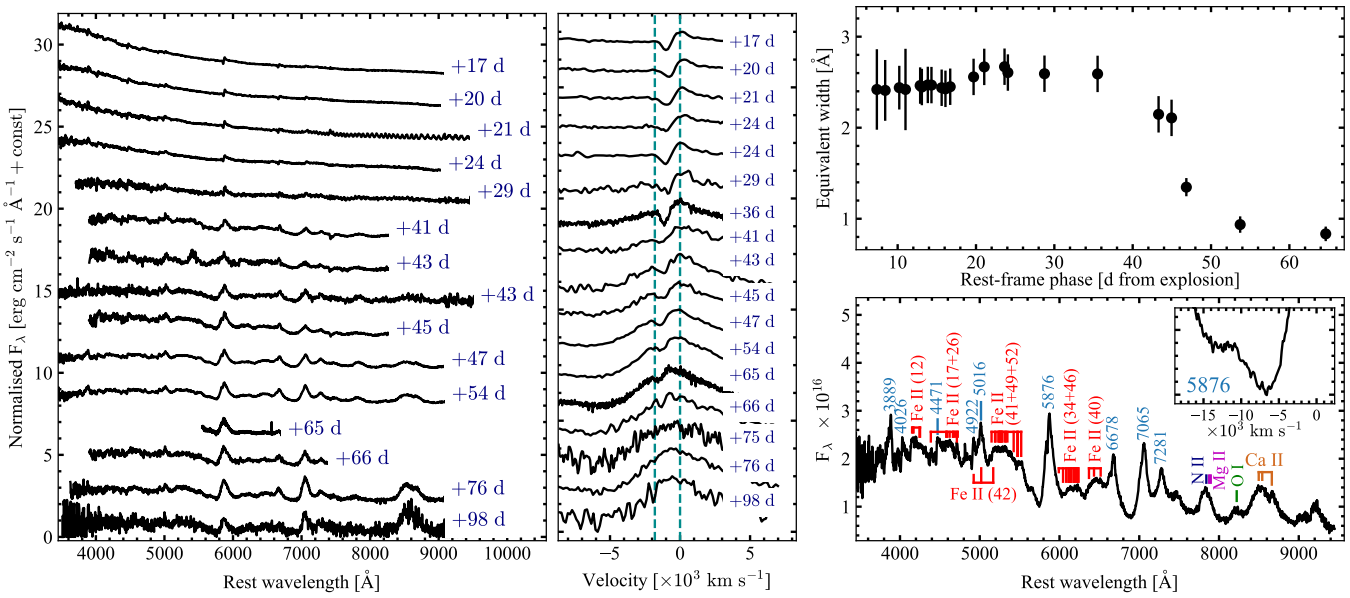


Fig. 10. *Left*: spectroscopic evolution of SN 2020able at $t > +17$ days. *Middle*: zoomed-in view around He I λ5876 showing the evolution of its narrow absorption feature. *Top right*: evolution of the EW of the He I λ5876 narrow absorption showing a sudden drop at $t \gtrsim +47$ days. *Bottom right*: line identification in the +47 days spectrum, with a zoomed-in view of the complex broad absorption feature observed in the He I λ5876 line. Rest-frame phases refer to the estimated epoch of the explosion.

explosion of SN 2006jc (Pastorello et al. 2007; Foley et al. 2007). We thus suggest that at least a fraction of the outer shell was produced by an eruptive episode, whereas a more extended CSM was generated by the wind of a WR star.

The evolution of the high-ionisation lines indicates that this inner denser shell is not reached by the fast ejecta ($v_{\rm ej} \simeq 6.7 \times 10^3$ km s^{-1}) in the first 16 days after the explosion. This allowed us to estimate a lower limit for its radius at $R_{\rm in,dense} \simeq 9.3 \times 10^{14}$ cm, which is compatible with the photospheric radius estimated by the SED fitting (see Sect. 2.2). On the other hand, the evolution of the EW of the He I P Cygni profiles indicates that the outer shell has an inner radius of $R_{\rm in} \simeq 2.2 \times 10^{15}$ cm. This implies a thickness of $\Delta R \lesssim 1.3 \times 10^{15}$ cm for the denser shell. With $\tau_{\rm es} = 6.5$ and a filling factor $f = 0.1$, this results in a density of $n_{\rm e} \simeq 7.5 \times 10^8$ cm^{-3} and a mass of approximately 0.02 M$_\odot$. Consequently, an eruptive episode of similar duration to that observed in SN 2006jc (10 days) with these physical properties must have had an average mass-loss rate of approximately 0.7 M$_\odot$ yr^{-1}. Given that eruptive events of evolved massive stars are not expected to exceed the expansion velocity of their steady winds significantly (Smith 2014), we were able to estimate the energetics of the outburst by assuming an expansion velocity of approximately 1.5×10^3 km s^{-1}. This would yield a substantial kinetic luminosity of $L_{\rm mech} = 1/2\, \dot{M}\, v_{\rm out}^2 \simeq 4.7 \times 10^{41}$ erg s^{-1}, assuming the mass-loss rate of 0.7 M$_\odot$ yr^{-1} derived above. To reconcile this with the archival non-detection limits ($M_{\rm bol} \geq -14.0$ mag, assuming a g-band bolometric correction of -0.3 mag, which is consistent with an outburst with a photospheric temperature between 10^4 and 1.2×10^4 K), a radiative efficiency of $\epsilon = L_{\rm bol}/L_{\rm mech} \lesssim 26\%$ is required. Although the relatively high optical depth suggests efficient thermalisation of the kinetic energy, this radiative efficiency remains physically consistent with the value of $\tau_{\rm es} = 6.5$ derived from the electron-scattering profiles. In addition, a filling factor of $f = 0.1$ reflecting the clumpy nature of the medium can limit the overall conversion efficiency, as a significant fraction of the kinetic energy can flow through the inter-clump medium without being thermalised.

At $t \gtrsim +46$ days, we also identified broad lines (FWHM $\simeq 5.0 \times 10^3$ km s^{-1}) of Ca II (near infrared triplet) and O I λ8222, along with numerous relatively narrow Fe II lines. The latter form the blends responsible for the blue pseudo-continuum at $\lambda \lesssim 5600$ Å, frequently observed in the spectra of interacting SNe (see Dessart et al. 2016). At approximately 7800 Å, we also observed a strong emission that was not easily identifiable. Its peak is inconsistent with Mg II $\lambda\lambda$7877, 7896, which would require a blueshift of approximately 2.0×10^3 km s^{-1}. Similarly, the O I λ7774 multiplet would be redshifted by about 2.4×10^3 km s^{-1}. Such shifts were not observed in any other broad line within the spectrum. Furthermore, we can exclude Fe II λ7841 – typically one of the most intense lines of multiplet 73 – as we do not detect other lines from the same multiplet, which should have comparable intensity (e.g. λ7712 and λ7320). A possible alternative identification is N II multiplet 11, which has a relatively intense line at 7841.27Å (see Fig. 10). The presence of nitrogen could be linked to the nature of the progenitor; in WN stars, nitrogen is indeed the second most abundant element after helium, which is a primary product of the CNO cycle. Wind velocities measured from the P Cygni minima of the He I lines would also be consistent with a WR progenitor in the WN/C transition phase.

In Fig. 11, we compare the spectral evolution of SN 2020able at $t > 43$ days with non-local-thermodynamic-equilibrium (LTE) radiative-transfer models. For each spectrum, we considered the best-fit model through a χ^2 minimisation algorithm against the full grid of models computed by Dessart et al. (2022). These represent low-mass helium stars with initial helium core masses – after the removal of the hydrogen envelope – of 3.3–5.0 M$_\odot$ evolved in interacting binary systems. Such progenitors are characterised by a high fractional helium abundance (typically ≥50%), which is essential to reproduce the persistence of He I emission lines observed in the data. In these simulations,

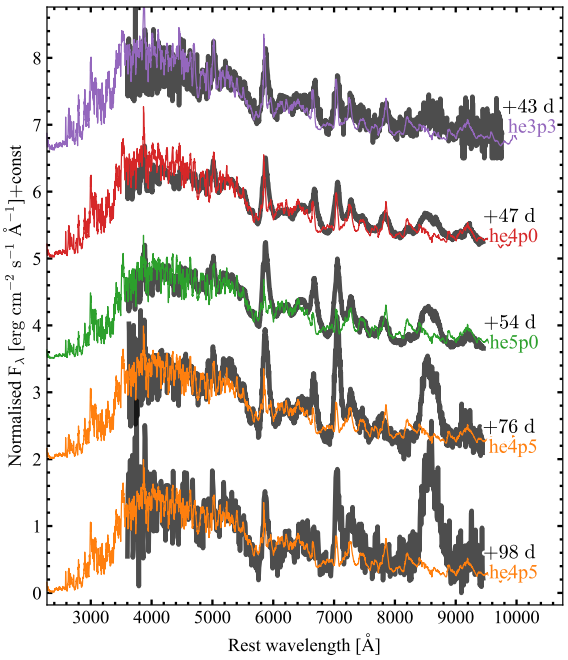


Fig. 11. Comparison of optical spectra of SN 2020able with non-LTE radiative-transfer models from Dessart et al. (2022). Spectra were normalised to their flux at 5500 Å.

parameters such as the radius of the cold dense shell (CDS), the mass accumulated within the CDS, and the power deposition from the ejecta–CSM interaction ($2.0–1.0 \times 10^{42}$ erg s^{-1}) are variables dependent on time. Consequently, the shifting agreement between each observed spectrum and specific model (i.e. from HE3P3 to HE4P5) does not imply a change in the underlying progenitor, but rather it captures the physical evolution of the spectrum-formation region as the CDS expands and the ionisation state of the gas evolves. Although the χ^2 procedure suggests a good agreement with the HE3P3-HE5P0 models – pointing towards a progenitor with a total ejected mass between 1.15 and 1.90 $M_\odot$ and a helium mass of 0.92–1.10 $M_\odot$ – a significant discrepancy remains in the observed line profiles. Specifically, the models fail to reproduce the broad emission and absorption components clearly visible in the spectra of SN 2020able. This mismatch likely arises from the fundamental assumptions of the Dessart et al. (2022) simulations, which were specifically designed to explore the spectral signatures of a CDS formed through strong ejecta–CSM interaction. In this regime, the compression of material into a narrow velocity space naturally produces the narrow lines characteristic of Type Ibn SNe. Since the spectrophotometric evolution of SN 2020able suggests that at these phases the interaction power is no longer the dominant energy source, the observed broad features likely originate from the inner SN ejecta now fully exposed. Consequently, while the models provide a fundamental benchmark for the chemical signature of Type Ibn SNe, the dynamical evidence in SN 2020able supports a higher mass progenitor channel, where the ejecta maintain a complex velocity stratification typical of massive stripped-envelope stars.

3. Summary and conclusions

In this paper, we discuss the UV/optical spectrophotometric evolution of the Type Ibn SN 2020able. The transient exploded in an environment with significantly subsolar metallicity, with an estimated 12 + log(O/H) = 8.28 ± 0.03 dex.

The early photospheric evolution highlights the need for a source of energy in addition to canonical recombination and radioactive decays. The combined information obtained from the early SED fitting, the observed deviation from a t^{-2} power-law evolution of *gri*-band light curves and the fit with MOSFiT indicates that the interaction must be geometrically and temporally confined to the very early post-explosion phases. In addition, the analysis of observed data indicates a stratified environment with three distinct regions at different distances from the progenitor star. For the innermost shocked shell, the best-fit MOSFiT parameters ($M_{\rm CSM} \simeq 0.6\,M_\odot$, $\rho \simeq 9.3 \times 10^{-9}$ g cm^{-3}, and $R_0 \simeq 3.7 \times 10^{12}$ cm) imply a remarkably compact outer radius of $R_{\rm out,shocked} \simeq 3.1 \times 10^{13}$ cm. This shell is likely fully ionised and does not contribute to the early spectroscopic evolution of SN 2020able, which is dominated by relatively narrow high-ionisation lines originating from an outer dense shell at $R_{\rm in,dense} \gtrsim 9.3 \times 10^{14}$ cm with $\tau_{es} \simeq 6.5$. The subsequent conversion of kinetic energy into radiation contributes significantly to the early excess observed in the *gri*-band light curves, as well as the relatively high peak luminosity (4.4×10^{43} erg s^{-1}), while at later phases it does not seem to contribute significantly to the energy output and spectroscopic evolution of the transient.

At a distance of $R_{in} \gtrsim 9.3 \times 10^{14}$ cm, the CSM exhibits a significant Thomson optical depth ($\tau_e \simeq 6.5$), as indicated by the FWHM of the electron scattering profiles, resulting in an average density of $n_{\rm e} \simeq 1.4 \times 10^9$ cm^{-3}. However, the expansion velocity of $v \simeq 1.2 \times 10^3$ km s^{-1}, derived from the P Cygni minima of He I and N III λ4100, is typical of steady winds of late WN to WC-type WR stars. This kinematic evidence is in stark contrast with the high mass-loss rate inferred from our density constraints. To maintain such a density and optical depth, a steady-state wind would require a mass-loss rate ($\dot{M} \simeq 8.7 \times 10^{-2}\,M_\odot$ yr^{-1}) that is physically inconsistent with radiation-driven wind theory for WR stars (Smith & Owocki 2006). We therefore conclude that at least the inner part of the un-shocked CSM was produced by a discrete pre-SN eruptive event, similar to that observed for SN 2006jc.

The discrepancy between the 'standard' velocity and the 'extreme' density can be reconciled by a steep density gradient within the un-shocked shell, where the bulk of the scattering mass ($M_{\rm dense} \simeq 1.8 \times 10^{-2}\,M_\odot$) is concentrated near the inner radius (at $R_{\rm in,dense} \gtrsim 9.3 \times 10^{14}$ cm), while the P Cygni profiles arise from the lower density outer layers produced by the steady wind of a WR star. The evolution of the EW of narrow absorptions further suggests that the inner and outer radii of the outermost shell must be approximately 2.2×10^{15} and 3.3×10^{15} cm, respectively, highlighting a complex stratified environment that mirrors the erratic terminal mass-loss history of its progenitor.

Assuming a 30% radiative efficiency (consistent with $\tau = 6.5$ estimated from electron-scattering profiles) and a filling factor of $f = 0.1$ (see Flores et al. 2023), the conversion of kinetic energy into radiation produced by the interaction of the ejecta with the denser shell would yield a luminosity of $L_{\rm int} = 1/2\,\epsilon\, f\, \dot{M}\, v_{\rm rel}^3 / v_{\rm shell} \simeq 5.8 \times 10^{41}$ erg s^{-1} (where we assumed $v_{shell} = 1.5 \times 10^3$ km s^{-1} $\gtrsim$ $v_{\rm wind}$; e.g. Smith 2014). With these assumptions, the interaction power would represent only a minor fraction (2–3%) of the bolometric luminosity at +16 days ($L_{\rm bol} = 2.45 \times 10^{43}$ erg s^{-1}) calculated in Sect. 2.2. Even assuming a higher radiative efficiency, a dense medium confined between 9.3×10^{14} and 2.2×10^{15} cm would be traversed by a shock at a relative velocity of 5.2×10^3 km s^{-1} in approximately 29 days. The ejecta–shell interaction would therefore be temporally confined within the first 45 days

post-explosion, assuming the shell is reached at $t \gtrsim +16$ days. This is in agreement with the spectroscopic evolution of the transient at $t \gtrsim +16$ days and $t \gtrsim +43$ days (see Sect. 2.3). A compact shell would increase the contribution of the interaction to the total luminosity of the transient (in any case $\lesssim$24%, assuming $f = 1$ and a 30% efficiency), but this scenario is inconsistent with the observations. Specifically, the fast photometric evolution, the lack of shocked components in the line profiles (e.g. intermediate-width boxy profiles), and the high ejecta velocities measured at +43 days (see Fig. 10) suggest a highly fragmented dense shell and a marginal impact of the interaction on the total bolometric luminosity at these phases. This is also highlighted by the comparison with the non-LTE radiative-transfer models of Dessart et al. (2022) (see our Fig. 11), which fail to reproduce the broad spectral features observed in SN 2020able at $t \gtrsim +43$ days. Although these models assume a spectrum dominated by a narrow-line-forming CDS, the mismatch suggests that ejecta–CSM interaction is not the primary driver of the spectroscopic evolution of the transient at these phases. The presence of broad features suggests that the inner, high-velocity ejecta have become the dominant source of emission, also supporting a more massive progenitor scenario characterised by the steep velocity gradients typical of stripped-envelope stars.

A consistent and detailed study of interaction processes in optical transients is of paramount importance, providing key parameters for deciphering the elusive final stages of massive star evolution, whilst also serving the field of multi-messenger astronomy. Such analyses are instrumental in mapping the diverse mass-loss histories of these progenitors, allowing us to bridge the gap between their late-stage instabilities and the diversity of observed cosmic explosions. Furthermore, providing tight constraints on the physical conditions within these environments is essential for identifying which transients possess the characteristics required to accelerate particles to relativistic velocities and efficiently produce high-energy neutrinos.

Data availability

Data shown in Figs. 2, 8 and 10 and the full Table 1 are available at the CDS via https://cdsarc.cds.unistra.fr/viz-bin/cat/J/A+A/715/A39. Light curves for the CSM and corner plots for the DEFAULT and CSM MOSFiT models are available at https://zenodo.org/records/21678623.

Acknowledgements. L.T., E.C., A.P., S.B., A.R., G.V., N.E.-R. and P.O. acknowledge support from the PRIN-INAF 2022 "Shedding light on the nature of gap transients: from the observations to the models". The Las Cumbres Observatory team is supported by NSF grants AST-2308113 and AST-1911151. Y.-Z.C is supported by the National Natural Science Foundation of China (No. 12303054), the Yunnan Fundamental Research Projects (Grant Nos. 202401AU070063, 202501AS070078), the National Key Research and Development Program of China (Grant No. 2024YFA1611603) and the International Centre of Supernovae, Yunnan Key Laboratory (No. 202302AN360001). G.V., A.R. and Y.-Z.C. also acknowledge financial support from the SOXS project (PI: S. Campana). N.E.R. also acknowledges the Spanish Ministerio de Ciencia e Innovación (MCIN) and the Agencia Estatal de Investigación (AEI) 10.13039/501100011033 under the program Unidad de Excelencia María de Maeztu CEX2020-001058-M. C.P.G. acknowledges financial support from grant RYC2024-050959-I, funded by MICIU/AEI/10.13039/501100011033 and the FSE+, as well as from projects PID2023-151307NB-I00, PIE 20215AT016, and CEX2020-001058-M, and the MaX-CSIC Excellence Award MaX4-SOMMA-ICE. B.K. is supported by the "Special Project for High-End Foreign Experts", Xingdian Funding from Yunnan Province and the National Key Research and Development Program of China (2024YFA1611603). D. acknowledges support from STFC grant No. ST/Y002253/1. Time-domain research by the University of Arizona team and D.J.S. is supported by National Science Foundation (NSF) grants 2308181, 2407566, and 2432036. ECSNOOPY is a package for SN photometry using PSF fitting developed by E. Cappellaro. A package description can be found at https://sngroup.oapd.inaf.it/ecsnoopy.html. Funding for the Sloan Digital Sky Survey IV has been provided by the Alfred P. Sloan Foundation, the U.S. Department of Energy Office of Science, and the Participating Institutions. SDSS-IV acknowledges support and resources from the Center for High Performance Computing at the University of Utah. The SDSS website is www.sdss.org. This work makes use of observations from the Las Cumbres Observatory network. Z.T.F. is a fully-automated, wide-field survey aimed at a systematic exploration of the optical transient sky, supported by the National Science Foundation under Grant Nos. AST-1440341 and AST-2034437 and a collaboration including current partners Caltech, IPAC, the Oskar Klein Centre at Stockholm University, the University of Maryland, University of California, Berkeley, University of Wisconsin at Milwaukee, University of Warwick, Ruhr University, Cornell University, Northwestern University and Drexel University. Operations are conducted by COO, IPAC, and UW. This research made use of the Spanish Virtual Observatory project, the NASA/IPAC Extragalactic Database (NED) and the HyperLeda database. Based on observations collected with the Copernico and Schmidt telescopes (Asiago, Italy) of the INAF – Osservatorio Astronomico di Padova. Data were in part obtained with ALFOSC, provided by the Instituto de Astrofisica de Andalucia (IAA) under a joint agreement with the University of Copenhagen and NOT. The Liverpool Telescope is operated on the island of La Palma by Liverpool John Moores University in the Spanish Observatorio del Roque de los Muchachos of the Instituto de Astrofisica de Canarias with financial support from the UK Science and Technology Facilities Council. Some observations reported here were obtained at the MMT Observatory, a joint facility of the University of Arizona and the Smithsonian Institution. Based on observations obtained at the 3.6 m Devasthal Optical Telescope (DOT), a National Facility run and managed by Aryabhatta Research Institute of Observational Sciences (ARIES), an autonomous Institute under the Department of Science and Technology, Government of India. The IAO facilities are operated by the Indian Institute of Astrophysics, Bangalore.

References

Abdurro'uf, Accetta, K., Aerts, C., et al. 2022, ApJS, 259, 35
Alam, S., Albareti, F. D., Allende Prieto, C., et al. 2015, ApJS, 219, 12
Alloin, D., Collin-Souffrin, S., Joly, M., & Vigroux, L. 1979, A&A, 78, 200
Angel, J. R. P., Hilliard, R. L., & Weymann, R. J. 1979, in The MMT and the Future of Ground-Based Astronomy, 385, ed. T. C. Weekes, 87
Arnett, W. D. 1980, ApJ, 237, 541
Arnett, W. D. 1982, ApJ, 253, 785
Asplund, M., Grevesse, N., Sauval, A. J., & Scott, P. 2009, ARA&A, 47, 481
Bellm, E. C., Kulkarni, S. R., Graham, M. J., et al. 2019, PASP, 131, 018002
Brown, P. J., Holland, S. T., Immler, S., et al. 2009, AJ, 137, 4517
Brown, T. M., Baliber, N., Bianco, F. B., et al. 2013, PASP, 125, 1031
Bruch, R. J., Gal-Yam, A., Yaron, O., et al. 2023, ApJ, 952, 119
Cai, Y.-Z., Pastorello, A., Maeda, K., et al. 2026, A&A, 707, A157
Chambers, K. C., Magnier, E. A., Metcalfe, N., et al. 2016, arXiv e-prints [arXiv:1612.05560]
Chatzopoulos, E., Wheeler, J. C., Vinko, J., Horvath, Z. L., & Nagy, A. 2013, ApJ, 773, 76
Chevalier, R. A., & Fransson, C. 1994, ApJ, 420, 268
Chonis, T. S., & Gaskell, C. M. 2008, AJ, 135, 264
Clocchiatti, A., Wheeler, J. C., Benetti, S., & Frueh, M. 1996, ApJ, 459, 547
Crowther, P. A. 2007, ARA&A, 45, 177
Crowther, P. A., De Marco, O., & Barlow, M. J. 1998, MNRAS, 296, 367
Denicoló, G., Terlevich, R., & Terlevich, E. 2002, MNRAS, 330, 69
Dessart, L., Hillier, D. J., Audit, E., Livne, E., & Waldman, R. 2016, MNRAS, 458, 2094
Dessart, L., Yoon, S.-C., Aguilera-Dena, D. R., & Langer, N. 2020, A&A, 642, A106
Dessart, L., Hillier, D. J., & Kuncarayakti, H. 2022, A&A, 658, A130
Dong, Y., Tsuna, D., Valenti, S., et al. 2024, ApJ, 977, 254
Fabricant, D., Fata, R., Epps, H., et al. 2019, PASP, 131, 075004
Filippenko, A. V. 1997, ARA&A, 35, 309
Fixsen, D. J., Cheng, E. S., Gales, J. M., et al. 1996, ApJ, 473, 576
Flores, B. L., Hillier, D. J., & Dessart, L. 2023, MNRAS, 518, 5001
Foley, R. J., Smith, N., Ganeshalingam, M., et al. 2007, ApJ, 657, L105
Fransson, C., Ergon, M., Challis, P. J., et al. 2014, ApJ, 797, 118
Gal-Yam, A., Arcavi, I., Ofek, E. O., et al. 2014, Nature, 509, 471
Gal-Yam, A., Bruch, R., Schulze, S., et al. 2022, Nature, 601, 201
Galbany, L., Stanishev, V., Mourão, A. M., et al. 2016, A&A, 591, A48
Gangopadhyay, A., Misra, K., Hiramatsu, D., et al. 2020, ApJ, 889, 170
Gangopadhyay, A., Misra, K., Hosseinzadeh, G., et al. 2022, ApJ, 930, 127
Gangopadhyay, A., Sollerman, J., Tsalapatas, K., et al. 2026, MNRAS, 547, staf1517

Gehrels, N., & Swift. 2004, in American Astronomical Society Meeting Abstracts, 205, American Astronomical Society Meeting Abstracts, 116.01
Gorbikov, E., Gal-Yam, A., Ofek, E. O., et al. 2014, MNRAS, 443, 671
Graham, M. J., Kulkarni, S. R., Bellm, E. C., et al. 2019, PASP, 131, 078001
Groh, J. H. 2014, A&A, 572, L11
Guillochon, J., Nicholl, M., Villar, V. A., et al. 2018, ApJS, 236, 6
Güver, T., & Özel, F. 2009, MNRAS, 400, 2050
Hakobyan, A. A., Mamon, G. A., Petrosian, A. R., Kunth, D., & Turatto, M. 2009, A&A, 508, 1259
Heger, A., Fryer, C. L., Woosley, S. E., Langer, N., & Hartmann, D. H. 2003, ApJ, 591, 288
Hiramatsu, D., Hosseinzadeh, G., Burke, J., et al. 2020, TNS Classification Report, 2020-3728, 1
Hosseinzadeh, G., Arcavi, I., Valenti, S., et al. 2017, ApJ, 836, 158
Hosseinzadeh, G., McCully, C., Zabludoff, A. I., et al. 2019, ApJ, 871, L9
Huang, C., & Chevalier, R. A. 2018, MNRAS, 475, 1261
Jiang, B., Jiang, S., & Ashley Villar, V. 2020, RNAAS, 4, 16
Joshi, Y. C., Bangia, T., Jaiswar, M. K., et al. 2022, JAI, 11, 2240004
Kansky, J., Chilingarian, I., Fabricant, D., et al. 2019, PASP, 131, 075005
Karamehmetoglu, E., Taddia, F., Sollerman, J., et al. 2017, A&A, 602, A93
Karamehmetoglu, E., Fransson, C., Sollerman, J., et al. 2021, A&A, 649, A163
Kool, E. C., Karamehmetoglu, E., Sollerman, J., et al. 2021, A&A, 652, A136
Kumar, B., Omar, A., Maheswar, G., et al. 2018, Bull. Soc. Roy. Sci. Liege, 87, 29
Maeda, K., & Moriya, T. J. 2022, ApJ, 927, 25
Marino, R. A., Rosales-Ortega, F. F., Sánchez, S. F., et al. 2013, A&A, 559, A114
Masci, F. J., Laher, R. R., Rusholme, B., et al. 2019, PASP, 131, 018003
Matzner, C. D., & McKee, C. F. 1999, ApJ, 510, 379
Moore, C. 1945, Contrib. Princeton Univ. Observ., 20, 1
Morozova, V., Piro, A. L., Renzo, M., et al. 2015, ApJ, 814, 63
Nadyozhin, D. K. 1994, ApJS, 92, 527
Nagao, T., Kuncarayakti, H., Maeda, K., et al. 2023, A&A, 673, A27
Nasa High Energy Astrophysics Science Archive Research Center (Heasarc). 2014, HEAsoft: Unified Release of FTOOLS and XANADU, Astrophysics Source Code Library [record ascl:1408.004]
Nomoto, K. I., Iwamoto, K., & Suzuki, T. 1995, Phys. Rep., 256, 173
Omar, A., Reddy, B. K., Kumar, T., & Pant, J. 2019, Bull. Soc. Roy. Sci. Liege, 88, 31
Osterbrock, D. E., & Ferland, G. J. 2006, Astrophysics of Gaseous Nebulae and Active Galactic Nuclei (University Science Books)
Panchal, D., Kumar, T. S., Omar, A., & Misra, K. 2023, JATIS, 9, 018002
Pastorello, A., Smartt, S. J., Mattila, S., et al. 2007, Nature, 447, 829
Pastorello, A., Mattila, S., Zampieri, L., et al. 2008, MNRAS, 389, 113
Pastorello, A., Benetti, S., Bufano, F., et al. 2011, AN, 332, 266
Pastorello, A., Benetti, S., Brown, P. J., et al. 2015a, MNRAS, 449, 1921
Pastorello, A., Hadjiyska, E., Rabinowitz, D., et al. 2015b, MNRAS, 449, 1954
Pastorello, A., Prieto, J. L., Elias-Rosa, N., et al. 2015c, MNRAS, 453, 3649
Pastorello, A., Tartaglia, L., Elias-Rosa, N., et al. 2015d, MNRAS, 454, 4293
Pastorello, A., Wyrzykowski, Ł., Valenti, S., et al. 2015e, MNRAS, 449, 1941
Pastorello, A., Wang, X. F., Ciabattari, F., et al. 2016, MNRAS, 456, 853
Paturel, G., Andernach, H., Bottinelli, L., et al. 1997, A&AS, 124, 109
Paturel, G., Fang, Y., Petit, C., Garnier, R., & Rousseau, J. 2000, A&AS, 146, 19
Pellegrino, C., Howell, D. A., Terreran, G., et al. 2022, ApJ, 938, 73
Pellegrino, C., Modjaz, M., Takei, Y., et al. 2024, ApJ, 977, 2
Perley, D. A., Sollerman, J., Schulze, S., et al. 2022, ApJ, 927, 180
Poznanski, D., Prochaska, J. X., & Bloom, J. S. 2012, MNRAS, 426, 1465
Prabhu, T. P. 2014, Proc. Indian Natl. Sci. Acad. Part A, 80, 887
Pursiainen, M., Leloudas, G., Schulze, S., et al. 2023, ApJ, 959, L10
Riess, A. G., Filippenko, A. V., Li, W., et al. 1999, AJ, 118, 2675
Sanders, N. E., Soderberg, A. M., Foley, R. J., et al. 2013, ApJ, 769, 39
Schlafly, E. F., & Finkbeiner, D. P. 2011, ApJ, 737, 103
Science Software Branch at STScI. 2012, PyRAF: Python alternative for IRAF, Astrophysics Source Code Library [record ascl:1207.011]
Selvelli, P., Danziger, J., & Bonifacio, P. 2007, A&A, 464, 715
Shingles, L., Smith, K. W., Young, D. R., et al. 2021, TNS AstroNote, 7, 1
Shivvers, I., Groh, J. H., Mauerhan, J. C., et al. 2015, ApJ, 806, 213
Shivvers, I., Filippenko, A. V., Silverman, J. M., et al. 2019, MNRAS, 482, 1545
Smith, N. 2014, ARA&A, 52, 487
Smith, N., & Owocki, S. P. 2006, ApJ, 645, L45
Smith, N., Li, W., Filippenko, A. V., & Chornock, R. 2011, MNRAS, 412, 1522
Smith, K. W., Smartt, S. J., Young, D. R., et al. 2020, PASP, 132, 085002
Speagle, J. S. 2020, MNRAS, 493, 3132
Taddia, F., Stritzinger, M. D., Fransson, C., et al. 2020, A&A, 638, A92
Tartaglia, L. 2016, PhD thesis, Astronomical Observatory of Padua; University of Padua, Department of Physics and Astronomy
Tartaglia, L., Pastorello, A., Sollerman, J., et al. 2020, A&A, 635, A39
Tartaglia, L., Valerin, G., Pastorello, A., et al. 2025, A&A, 703, A177
Tody, D. 1986, in SPIE Conference Series, 627, Instrumentation in astronomy VI, ed. D. L. Crawford, 733
Tody, D. 1993, in Astronomical Society of the Pacific Conference Series, 52, Astronomical Data Analysis Software and Systems II, eds. R. J. Hanisch, R. J. V. Brissenden, & J. Barnes, 173
Tomasella, L., Cappellaro, E., Fraser, M., et al. 2013, MNRAS, 434, 1636
Tonry, J., Denneau, L., Heinze, A., et al. 2020, TNS Discovery Report, 2020-3630, 1
Villar, V. A., Berger, E., Metzger, B. D., & Guillochon, J. 2017, ApJ, 849, 70
Walborn, N. R. 1972, AJ, 77, 312
Wang, X., Lin, W., Zhang, J., et al. 2021, ApJ, 917, 97
Wang, Z. Y., Pastorello, A., Maeda, K., et al. 2024, A&A, 691, A156
Wang, Z.-Y., Pastorello, A., Cai, Y.-Z., et al. 2025, A&A, 700, A156
Warwick, B., Lyman, J., Pursiainen, M., et al. 2025, MNRAS, 536, 3588
Wu, C., Zha, S., Cai, Y., et al. 2024, ApJ, 967, L45
York, D. G., Adelman, J., Anderson, Jr., J. E., et al. 2000, AJ, 120, 1579

[1] INAF – Osservatorio Astronomico d'Abruzzo, Via Mentore Maggini s.n.c., 64100 Teramo, Italy
[2] INAF – Osservatorio Astronomico di Padova, Vicolo dell'Osservatorio 5, 35122 Padova, Italy
[3] INAF – Osservatorio Astronomico di Brera, Via E. Bianchi 46, 23807 Merate (LC), Italy
[4] Oskar Klein Centre, Department of Astronomy, Stockholm University, AlbaNova, 106 91 Stockholm, Sweden
[5] Aryabhatta Research Institute of Observational Sciences, Nainital-263001, India
[6] Physical Research Laboratory, Navrangpura, Ahmedabad, Gujarat 380009, India
[7] School of Physics and Astronomy, University of Birmingham, Edgbaston, Birmingham B15 2TT, UK
[8] Institute for Gravitational Wave Astronomy, University of Birmingham, Birmingham B15 2TT, UK
[9] South-Western Institute for Astronomy Research, Yunnan University, Kunming, Yunnan 650504, PR China
[10] Yunnan Key Laboratory of Survey Science, Yunnan University, Kunming, Yunnan 650500, PR China
[11] National Centre for Radio Astrophysics, Tata Institute of Fundamental Research, Post Bag 3, Ganeshkhind, Pune 411007, India
[12] Indian Institute of Astrophysics, Koramangala 2nd Block, Bangalore 560034, India
[13] Institute of Space Sciences (ICE, CSIC), Campus UAB, Carrer de Can Magrans, s/n, 08193 Barcelona, Spain
[14] Las Cumbres Observatory, 6740 Cortona Drive, Suite 102, Goleta, CA 93117-5575, USA
[15] Department of Physics, University of California, Santa Barbara, CA 93106-9530, USA
[16] Department of Astronomy, University of Florida, Bryant Space Science Center, Gainesville, FL 32611-2055, USA
[17] NASA Goddard Space Flight Center, 8800 Greenbelt Road, Greenbelt, MD 20771, USA
[18] Università degli Studi di Padova, Dipartimento di Fisica e Astronomia, Vicolo dell'Osservatorio 3, 35122 Padova, Italy
[19] Gemini Observatory/NSF's National Optical-Infrared Astronomy Research Laboratory, 670 N. Aohoku Place, Hilo, HI 96720, USA
[20] Steward Observatory, University of Arizona, 933 North Cherry Avenue, Tucson, AZ 85721-0065, USA
[21] Yunnan Observatories, Chinese Academy of Sciences, Kunming 650216, PR China
[22] International Centre of Supernovae, Yunnan Key Laboratory, Kunming 650216, PR China
[23] Department of Astronomy, The University of Texas at Austin, 2515 Speedway, Stop C1400, Austin, TX 78712, USA
[24] Department of Physics and Astronomy, Johns Hopkins University, Baltimore, MD 21218, USA
[25] Independent researcher, Santa Barbara, CA, USA

Appendix A: Observations and data reduction

A.1. Photometry

Photometric followup started soon after the ATLAS discovery (see Sect. 1), with early Near ultra-violet (UV; $\sim$ 1600 – 4700 Å) and *UBV* observations carried out using the 0.3 m Ultra-Violet Optical Telescope (UVOT) on board the Swift Gamma Ray Burst Explorer (Gehrels & Swift 2004). The corresponding apparent UV/optical magnitudes were obtained following the prescription of Brown et al. (2009) with HEASOFT v. 6.33 (Nasa High Energy Astrophysics Science Archive Research Center (Heasarc) 2014) on pre-processed images retrieved from the Swift archive[5]. Optical photometry was also obtained with facilities of the Las Cumbres Observatory network (Brown et al. 2013) within the Global Supernova Project (GSP), as well as the 2.56 m Nordic Optical Telescope (NOT) equipped with the "Alhambra Faint Object Spectrograph and Camera" (ALFOSC[6]), the 2 m Liverpool Telescope (LT) with the "Infrared-Optical: Optical" (IO:O) camera, the 1.82 m Copernico telescope with the "Asiago Faint Object Spectrograph and Camera" (AFOSC) and the 69/92 cm Schmidt with a G4-16000LC Moravian camera of the Asiago observatory (Mount Ekar), all within the NOT Unbiased Transient Survey 2 (NUTS2[7]). Additional *ugriz* photometry was obtained with the 1.3 m Devasthal Fast Optical Telescope (DFOT; Joshi et al. 2022) and the 3.6 m Devasthal Optical Telescope (DOT; Kumar et al. 2018). Publicly available ZTF *gri* frames obtained with the Samuel Oschin 1.2 m (48 inches) Telescope (Palomar 48 – P48) were retrieved from the NASA/IPAC Infrared Science Archive[8]. All of these data were reduced using the superNOva photometry (ECSNOOPY[9]) pipeline, which is based on point spread function (PSF) fitting and zero-point calibration using stars from the Sloan Digital Sky Survey (SDSS) catalogue (Data Release 17 – DDR17; Abdurro'uf et al. 2022). Additional details on the reduction steps within ECSNOOPY are given in Tartaglia (2016). ATLAS light curves obtained in *orange* and *cyan* bands (*o* and *c*, respectively) were retrieved using the ATLAS Forced Photometry server for public use (Shingles et al. 2021). UV and *UBV* magnitudes were calibrated in the Vega photometric system, applying the transformations derived by Chonis & Gaskell (2008) to the *ugriz* magnitudes of the stars in the field to compute the proper zero points. *ugcroiz* magnitudes were calibrated in the AB photometric system.

A.2. Spectroscopy

The spectroscopic follow-up started on 2020 December 8.5 UT (JD = 2459192.0), approximately 7 days after the estimated explosion (considering the rest-frame phase corrected for cosmological redshift). Data were collected within the GSP, using the 2 m Faulkes north and south telescopes of the Las Cumbres Observatory, located at the Haleakala Observatories (Faulkes Telescope North, Hawaii – USA; FTN) and the Siding Spring Observatory (Faulkes Telescope South, Australia; FTS) using the cross-dispersed, low-resolution spectrographs FLOYDS. These were reduced using their dedicated pipeline[10]. Spectra were also obtained using the 2.56 m NOT with ALFOSC and the 1.82 m Copernico telescope with AFOSC, both within the NUTS2 collaboration. Data obtained with ALFOSC and AFOSC were reduced using the FOSCGUI pipeline[11], which performs standard IRAF reduction steps (Tody 1986, 1993) through PYRAF (Science Software Branch at STScI 2012). Additional low- and medium-resolution spectra (see Table A.1) were obtained using DOT with ADFOSC (Omar et al. 2019; Panchal et al. 2023) and the 2 m Himalayan Chandra Telescope with the Hanle Faint Object Spectrograph Camera (HFOSC; Prabhu 2014), both processed through standard IRAF reduction steps. Three mid-resolution ($R \simeq 4000$) spectra were obtained using the 6.5 m MMT located at the Fred Lawrence Whipple Observatory in Arizona with Blue Channel and Binospec (Fabricant et al. 2019) spectrographs. Observations taken with Binospec (Fabricant et al. 2019) on MMT were initially processed using the Binospec IDL pipeline (Kansky et al. 2019) for flat-fielding, sky subtraction, and wavelength and flux calibrations. The 1D spectrum were then extracted using IRAF techniques (Tody 1986). Spectra obtained with BlueChannel (Angel et al. 1979) on MMT are reduced using standard IRAF techniques. An additional spectrum was obtained with the Boller & Chivens (B&C) spectrograph on the 2.3 m Bok telescope, located at the Kitt Peak National Observatory (KPNO) in Arizona, USA and reduced using standard IRAF routines. A log of the observations, including additional information on the instrumental setup used, is reported in Table A.1. After data reduction, absolute flux calibrations were checked against photometry obtained on the closest night, mostly by multiplying the spectral continuum by a constant. At early phases ($t \lesssim +10$ days), the spectral shape was corrected using low-order (1 or 2) polynomials, since the observed spectral continuum was too red with respect to the SED computed from the photometry.

[5] https://swift.gsfc.nasa.gov/archive/
[6] https://www.not.iac.es/instruments/alfosc/
[7] https://nuts.sn.ie/
[8] https://irsa.ipac.caltech.edu/Missions/ztf.html
[9] https://sngroup.oapd.inaf.it/ecsnoopy.html
[10] https://lco.global/documentation/data/floyds-pipeline/
[11] https://sngroup.oapd.inaf.it/foscgui.html

Table A.1. Log of the spectroscopic observations of SN 2020able.

Date	JD	Rest-frame phase	Telescope+Instrument	Grism/grating	Range	Resolution	Exposure
	(days)	(days)			(Å)	($\lambda/\Delta\lambda$)	(s)
20201208	2459191.99	+7	OGG2m+FLOYDS	red+blue	3500 – 10000	505	3600
20201209	2459193.07	+8	OGG2m+FLOYDS	red+blue	3500 – 10000	530	2700
20201211	2459194.95	+10	OGG2m+FLOYDS	red+blue	3500 – 10000	555	2700
20201212	2459195.74	+11	NOT+ALFOSC	Gr4	3700 – 9700	330	900
20201214	2459197.64	+13	Ekar182+AFOSC	Gr4	3400 – 9400	390	2×1800
20201213	2459197.39	+13	MMT+BCH	1200GPM/LP-530	5700 – 7000	4000	3×600
20201215	2459198.65	+14	NOT+ALFOSC	Gr4	3700 – 9700	410	2×1800
20201215	2459199.13	+14	OGG2m+FLOYDS	red+blue	3500 – 10000	520	2700
20201216	2459200.46	+16	Ekar182+AFOSC	VPH6+VPH7	3700 – 9400	400	1800 + 1800
20201217	2459200.96	+16	OGG2m+FLOYDS	red+blue	3500 – 10000	510	2700
20201218	2459201.59	+17	NOT+ALFOSC	Gr4	3700 – 9700	400	1800
20201221	2459204.65	+20	NOT+ALFOSC	Gr4	3700 – 9700	330	1800
20201222	2459206.04	+21	OGG2m+FLOYDS	red+blue	3500 – 10000	525	2700
20201225	2459208.70	+24	NOT+ALFOSC	Gr4	3700 – 9700	290	2400
20201230	2459213.92	+29	OGG2m+FLOYDS	red+blue	3500 – 10000	520	2700
20210105	2459220.40	+36	MMT+BCH	1200GPM/LP-530	5700 – 7000	4000	3×600
20210107	2459221.53	+36	DOT+ADFOSC	676R/RG-610	6100 – 8200	1100	2×900
20210111	2459226.45	+41	DOT+ADFOSC	676R	4000 – 9000	620	3×900
20210114	2459228.61	+43	DOT+ADFOSC	676R	4000 – 9000	620	3×900
20210114	2459228.86	+43	OGG2m+FLOYDS	red+blue	3500 – 10000	540	2700
20210116	2459230.58	+45	DOT+ADFOSC	676R	4000 – 9000	620	4×900
20210118	2459232.49	+47	NOT+ALFOSC	Gr4	3700 – 9700	430	2×1800
20210125	2459239.54	+54	NOT+ALFOSC	Gr4	3700 – 9700	430	3600
20210204	2459250.24	+65	MMT+Binospec	×1000/LP3800	5700 – 7000	3900	5×600
20210206	2459251.78	+66	Bok+B&C	300g/mm	4000 – 8000	700	3×1200
20210215	2459261.12	+75	HCT+HFOSC	Gr7+Gr8	4000 – 9000	1330+2190	2700 + 2700
20210216	2459262.47	+76	NOT+ALFOSC	Gr4	3700 – 9700	400	3600
20210312	2459285.49	+98	NOT+ALFOSC	Gr4	3700 – 9700	420	3600

Notes. OGG2m: 2m0-01 telescope with FLOYDS at Las Cumbres Observatory node at Haleakala Observatory; NOT: 2.56 m Nordic Optical Telescope with ALFOSC; Ekar182: 1.82 m Copernico telescope with AFOSC; MMT: 6.5 m MMT with the Blue Channel and Binospec spectrographs; DOT: 3.6 m Devasthal Optical Telescope with the ARIES Devasthal Faint Object Spectrograph and Camera (ADFOSC); HCT: 2 m Himalayan Chandra Telescope with the Himalayan Faint Object Spectrograph and Camera (HFOSC). Rest-frame phases refer to the estimated epoch of the SN explosion.

Appendix B: Analysis of the early light curves of Type Ibn/Icn SNe

Table B.1. Data points used to produce Figs. 4 and 5.

SN	MJD_{expl} (err)	t_{rise} (err)	Decline (err)	μ	m_{abs} (err)	Filter	Type/subclass	Reference
	JD-2400000.5	(d)	(mag d^{-1})	(mag)	(mag)			
2010al	55267.5(1.5)	17.2(1.5)	0.0792(0.0020)	34.27(0.16)	−18.81(0.16)	*R*	HI	(1)
OGLE-2012-SN-006	56206.339(0.031)	11.276(0.061)	0.0477(0.0012)	36.94(0.18)	−19.65(0.18)	*I*	P Cygni	(2)
PTF12ldy	56236.190(0.047)	8.984(0.056)	0.130(0.012)	38.36(0.15)	−18.97(0.15)	*r*	P Cygni	(3)
PS1-12sk	55993.624(0.055)	12.559(0.064)	0.079(0.021)	36.75(0.15)	−18.80(0.15)	*z*	emission	(4)
iPTF13beo	56430.900(0.025)	2.843(0.072)	0.0575(0.0033)	38.01(0.15)	−18.41(0.15)	*r*	emission	(5)
LSQ13ccw	56534.879(0.014)	4.847(0.025)	0.134(0.012)	37.07(0.14)	−18.25(0.34)	*g*	emission	(6)
2014av	56763.277(0.056)	6.44(0.15)	0.1409(0.0090)	35.56(0.15)	−19.68(0.15)	*R*	Ibn	(7)
ASASSN-14ms	57014.99(0.25)	6.77(0.28)	0.0419(0.0034)	36.72(0.14)	−20.41(0.14)	*V*	Ibn	(8)
iPTF14aki	56756.359(0.026)	9.615(0.032)	0.1205(0.0018)	37.13(0.15)	−19.01(0.15)	*R*	emission	(3)
OGLE-2014-SN-131	56921.27(0.75)	48.5(1.6)	0.0089(0.0040)	37.85(0.15)	−18.08(0.15)	*I*	Ibn	(9)
ASASSN-15ed	57078.5(2.7)	8.5(3.8)	0.1159(0.0094)	36.59(0.14)	−19.98(0.34)	*r*	P Cygni	(10)
2015U	57062.598(0.073)	9.46(0.10)	0.1510(0.0020)	33.85(0.15)	−19.61(0.15)	*r*	P Cygni	(11)
iPTF15ul	57090.302(0.006)	4.2960(0.0078)	0.1824(0.0070)	37.18(0.15)	−19.40(0.15)	*g*	Ibn	(3)
2018bcc	58225.355(0.018)	5.403(0.032)	0.1476(0.0036)	37.19(0.15)	−19.41(0.15)	*r*	Ibn	(12)
2018jmt	58456.709(0.080)	8.26(0.19)	0.1140(0.0081)	35.65(0.22)	−19.13(0.22)	*g*	Ibn	(13)
2019cj	58483.54(0.18)	8.22(0.26)	0.0666(0.0072)	36.38(0.16)	−18.84(0.16)	*g*	HI	(13)
2019hgp	58640.982(0.035)	8.06(0.12)	0.0904(0.0028)	37.21(0.15)	−18.49(0.15)	*r*	Icn	(14)
2019jc	58489.42(0.13)	5.17(0.13)	0.106(0.025)	34.55(0.15)	−17.06(0.15)	*r*	Icn	(15)
2019uo	58499.578(0.067)	9.455(0.071)	0.1710(0.0023)	34.74(0.15)	−18.10(0.15)	*r*	HI	(16)
2020able	59183.96(0.43)	15.289(0.054)	0.0505(0.0016)	35.16(0.15)	−18.79(0.15)	*r*	HI	This work
2020bqj	58861.69(0.98)	37.7(1.1)	0.0068(0.0020)	37.92(0.15)	−19.90(0.15)	*r*	Ibn	(17)
2020nxt	59032.4830(0.0090)	6.482(0.012)	0.1638(0.0028)	34.80(0.03)	−18.999(0.030)	*o*	Ibn	(18)
2020taz	59098.11(0.15)	13.55(0.28)	0.0475(0.0060)	36.62(0.02)	−17.858(0.024)	*o*	Ibn	(18)
2021ckj	59251.88(0.48)	7.44(0.86)	0.1256(0.0082)	39.07(0.15)	−19.88(0.16)	*r*	Icn	(19,20)
2021csp	59251.43(0.32)	8.34(0.33)	0.0760(0.0028)	37.82(0.15)	−19.99(0.16)	*g*	Icn	(21)
2022ablq	59905.613(0.060)	10.951(0.066)	0.0940(0.0031)	33.87(0.15)	−19.46(0.15)	*g*	Ibn	(22)
2023emq	60033.315(0.030)	7.582(0.037)	0.236(0.020)	35.77(0.15)	−19.00(0.15)	*o*	HI	(23)
2023fyq	60147.913(0.049)	6.139(0.050)	0.14939(0.00038)	31.28(0.45)	−18.25(0.45)	*r*	Ibn	(24)
2023utc	60227.31(0.10)	7.15(0.11)	0.0707(0.0039)	33.80(0.46)	−16.35(0.46)	*r*	Ibn	(18)
2023tsz	60199.7(1.7)	13.8(1.7)	0.1201(0.0084)	35.35(0.15)	−19.45(0.21)	*g*	Ibn	(25)
2023xgo	60256.925(0.023)	4.954(0.080)	0.1531(0.0021)	33.678(0.056)	−17.661(0.057)	*r*	Icn	(26)
2024acyl	60644.78(0.23)	5.85(0.26)	0.0880(0.0054)	35.23(0.15)	−18.18(0.15)	*V*	Ibn	(27)
2024aej	60321.47(0.13)	7.10(0.14)	0.1417(0.0067)	37.17(0.11)	−19.22(0.11)	*r*	Ibn	(18)

Notes. HI: Type Ibn SNe showing high-ionisation features in their early spectra. The other labels refer to the sub-classification proposed by Hosseinzadeh et al. (2017)

References. (1) Pastorello et al. (2015a); (2) Pastorello et al. (2015e); (3) Hosseinzadeh et al. (2017); (4) Sanders et al. (2013); (5) Gorbikov et al. (2014); (6) Pastorello et al. (2015b); (7) Pastorello et al. (2016); (8) Wang et al. (2021); (9) Karamehmetoglu et al. (2017); (10) Pastorello et al. (2015c); (11) Pastorello et al. (2015d); (12) Karamehmetoglu et al. (2021); (13) Wang et al. (2024); (14) Gal-Yam et al. (2022); (15) Wu et al. (2024); (16) Gangopadhyay et al. (2020); (17) Kool et al. (2021); (18) Wang et al. (2025); (19) Pellegrino et al. (2022); (20) Nagao et al. (2023); (21) Perley et al. (2022); (22) Pellegrino et al. (2024); (23) Pursiainen et al. (2023); (24) Dong et al. (2024); (25) Warwick et al. (2025); (26) Gangopadhyay et al. (2026); (27) Cai et al. (2026)

Appendix C: Modelling of the light curves of SNe 2010al and 2020able with MOSFiT

Table C.1. Parameters of the DEFAULT analytical model obtained with MOSFiT for SNe 2010al and 2020able.

Parameter	Prior range	2010al	2020able	Unit
M_{ej}	$0.1 - 10.0$	$0.474^{+0.030}_{-0.026}$	$17.95^{+1.15}_{-1.88}$	$M_\odot$
$M_{^{56}Ni}$	$10^{-3} \times M_{ej} - 1.0 \times M_{ej}$	$0.461^{+0.031}_{-0.030}$	$15.67^{+1.84}_{-2.95}$	$M_\odot$
v_{ej}	$1.0 \times 10^3 - 1.0 \times 10^5$	8280^{+390}_{-370}	$(9.42^{+0.40}_{-0.71}) \times 10^4$	km s^{-1}
A_V	$4.5 \times 10^{-6} - 45$	$0.0002^{+0.0021}_{-0.0002}$	$0.79^{+0.04}_{-0.06}$	mag
T_{min}	$1.0 - 10^4$	2100^{+1000}_{-800}	22800^{+1000}_{-1300}	K
MJD_{expl}	$-10 - 0^a$	$55265.76^{+0.353}_{-0.373}$	$59182.961^{+0.163}_{-0.177}$	-

Notes. [a] The prior range refers to the phase with respect to the first detection. Corresponding light curves and corner plots showing the posterior probability distributions are available at https://zenodo.org/records/21678623

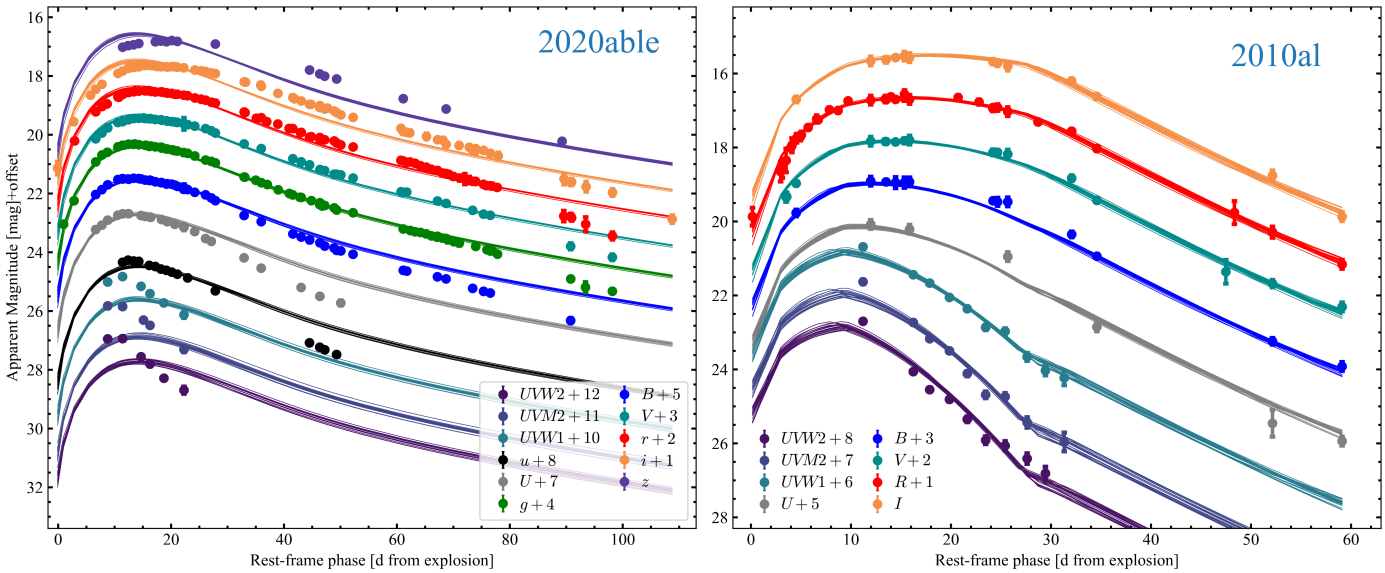


Fig. C.1. Multi-band light curves of SN 2020able (*left*) and SN 2010al (*right*) compared with an ensemble of MOSFiT models generated using the DEFAULT module, which implements a standard nickel-cobalt (^{56}Ni → ^{56}Co) radioactive decay power source without accounting for ejecta-CSM interaction. The model fails to reproduce the overall light curve evolution, particularly the early-time luminous peaks observed in the UV bands. Light curves have been vertically displaced by the indicated offsets for clarity. Rest-frame phases are relative to the estimated explosion epoch of each event.

Table C.2. Parameters of the CSMNI analytical model obtained with MOSFiT for SNe 2010al and 2020able.

Parameter	Prior range	2010al	2020able	Unit
E_k	$0.5 - 10.0$	$0.38^{+0.56}_{-0.49}$	$0.29^{+0.012}_{-0.013}$	10^{51} erg
$M_{\rm ej}$	$0.1 - 10.0$	$1.15^{+0.20}_{-0.17}$	$1.315^{+0.062}_{-0.068}$	$M_\odot$
n	$6 - 10$	$7.92^{+0.48}_{-0.44}$	$6.595^{+0.080}_{-0.068}$	-
$M_{^{56}\rm Ni}$	$10^{-3} \times M_{\rm ej} - 1.0 \times M_{\rm ej}$	$0.0065^{+0.0028}_{-0.0022}$	$0.0315^{+0.0043}_{-0.0038}$	$M_\odot$
R_0	$2.0 \times 10^{-3} - 25$	$0.110^{+0.74}_{-0.098}$	$0.25^{+0.32}_{-0.19}$	AU
$M_{\rm CSM}$	$0.1 - 10.0$	$0.490^{+0.023}_{-0.023}$	$0.573^{+0.013}_{-0.014}$	$M_\odot$
ρ_{CSM}	$10^{-16} - 10^{-6}$	$(4.17^{+367.37}_{-4.10}) \times 10^{-8}$	$(9.33^{+122.80}_{-7.50}) \times 10^{-9}$	g cm^{-3}
A_V	$4.5 \times 10^{-6} - 45$	$0.442^{+0.036}_{-0.043}$	$0.147^{+0.012}_{-0.013}$	mag
T_{min}	$1.0 - 10^4$	7762^{+18}_{-18}	7499^{+52}_{-52}	K
MJD$_{\rm expl}$	$-10 - 0^{\rm a}$	$55266.99^{+0.13}_{-0.15}$	$59183.433^{+0.083}_{-0.086}$	-

Notes. [a] The prior range refers to the phase with respect to the first detection.

Table C.3. Parameters of the CSM analytical model obtained with MOSFiT for SNe 2010al and 2020able.

Parameter	Prior range	2010al	2020able	Unit
$M_{\rm ej}$	$0.1 - 10.0$	$1.32^{+0.17}_{-0.18}$	$1.9055^{+0.0016}_{-0.0044}$	$M_\odot$
v_{ej}	$1.0 \times 10^3 - 1.0 \times 10^5$	7520^{+140}_{-137}	5.5×10^3 (fixed)	km s^{-1}
n	$6 - 10$	$9.29^{+0.42}_{-0.62}$	$6.79^{+0.07}_{-0.07}$	-
R_0	$2.0 \times 10^{-3} - 25$	$6.9^{+5.4}_{-3.6}$	$35.5^{+3.4}_{-3.1}$	AU
$M_{\rm CSM}$	$0.1 - 10.0$	$2.64^{+0.19}_{-0.16}$	$0.6918^{+0.0016}_{-0.0016}$	$M_\odot$
ρ_{CSM}	$10^{-16} - 10^{-6}$	$(7.6^{+25.0}_{-5.0}) \times 10^{-12}$	$(5.62^{+0.83}_{-0.73}) \times 10^{-13}$	g cm^{-3}
A_V	$4.5 \times 10^{-6} - 45^{\rm a}$	$0.412^{+0.034}_{-0.034}$	0.14 (fixed)	mag
T_{min}	$1.0 - 10^4$	7710^{+143}_{-140}	7460^{+190}_{-250}	K
MJD$_{\rm expl}$	$-10 - 0^{a}$	$55266.94^{+0.13}_{-0.14}$	$59182.6^{+0.13}_{-0.13}$	-

Notes. [a] The prior range refers to the phase with respect to the first detection. The corresponding light curves and corner plots showing the posterior probability distributions are available at https://zenodo.org/records/21678623

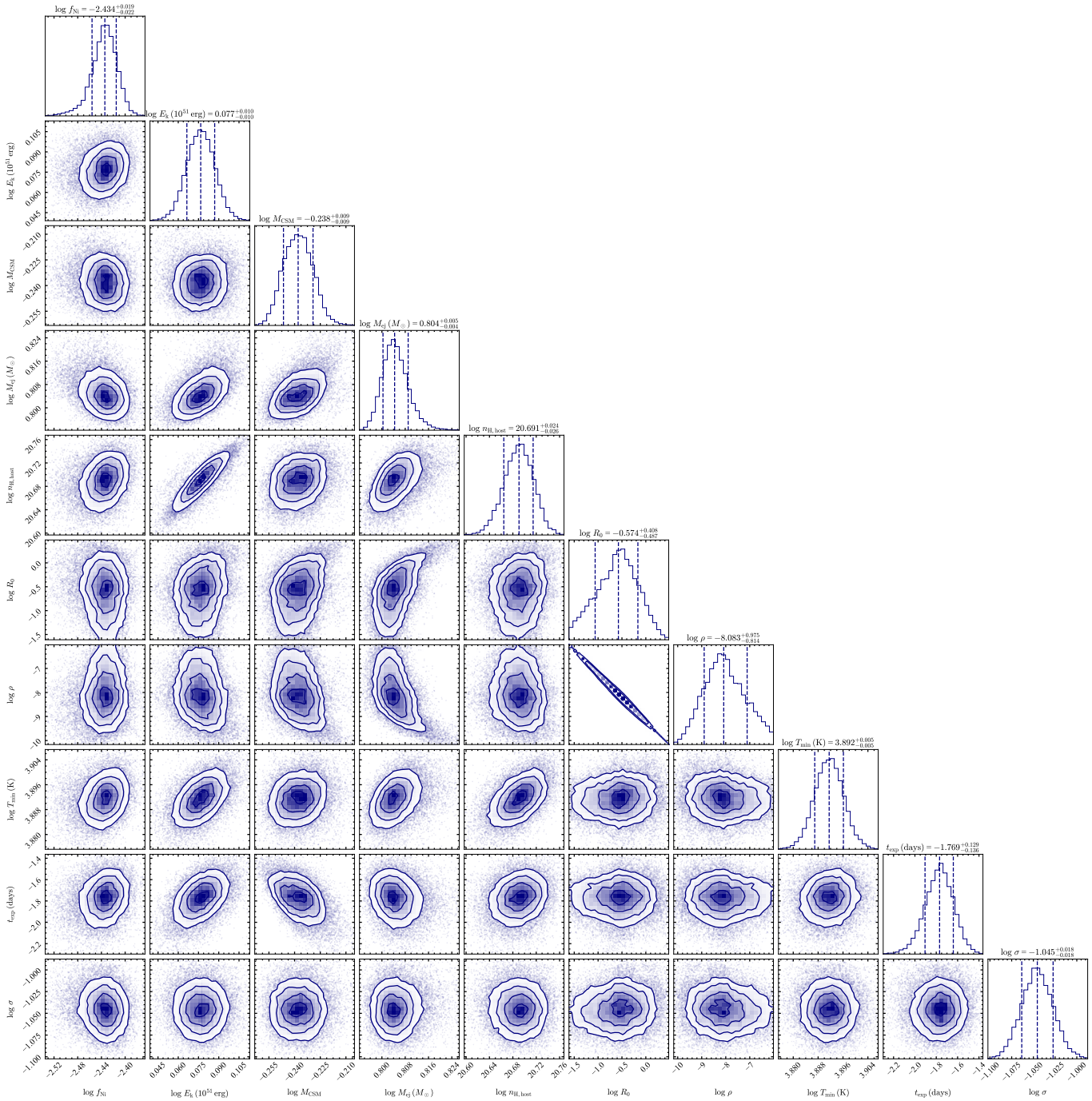


Fig. C.2. Posterior probability distributions for SN 2020able, generated by MOSFiT using the CSMNI model. The corner plot displays the multi-dimensional parameter space. Vertical dashed lines in the 1D histograms represent the median values and the 1σ confidence intervals.

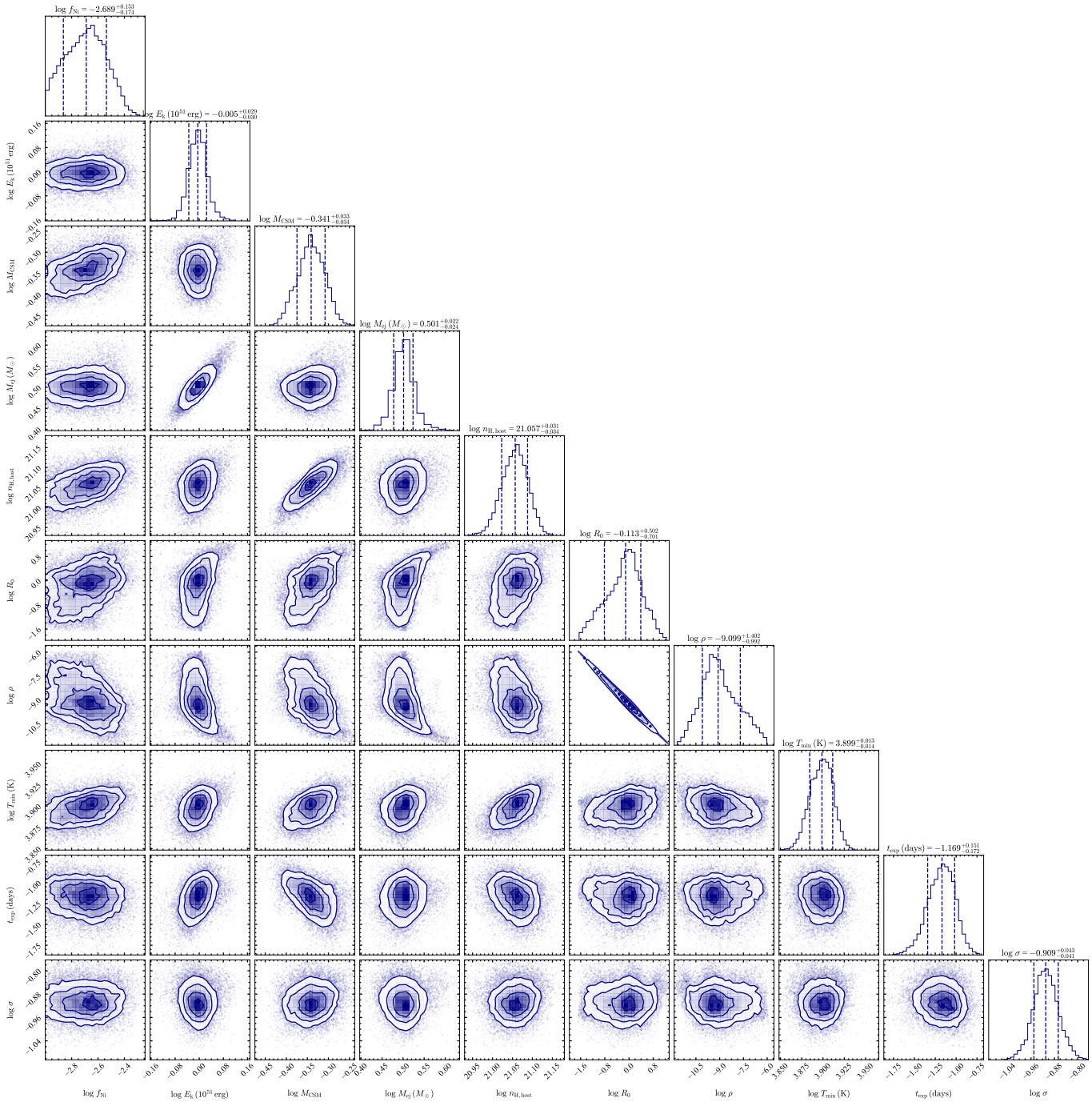


Fig. C.3. Same as Fig. C.2 but for SN 2010al.